Article

Cell Reports

GNA11 Q209L Mouse Model Reveals RasGRP3 as an Essential Signaling Node in Uveal Melanoma

Graphical Abstract

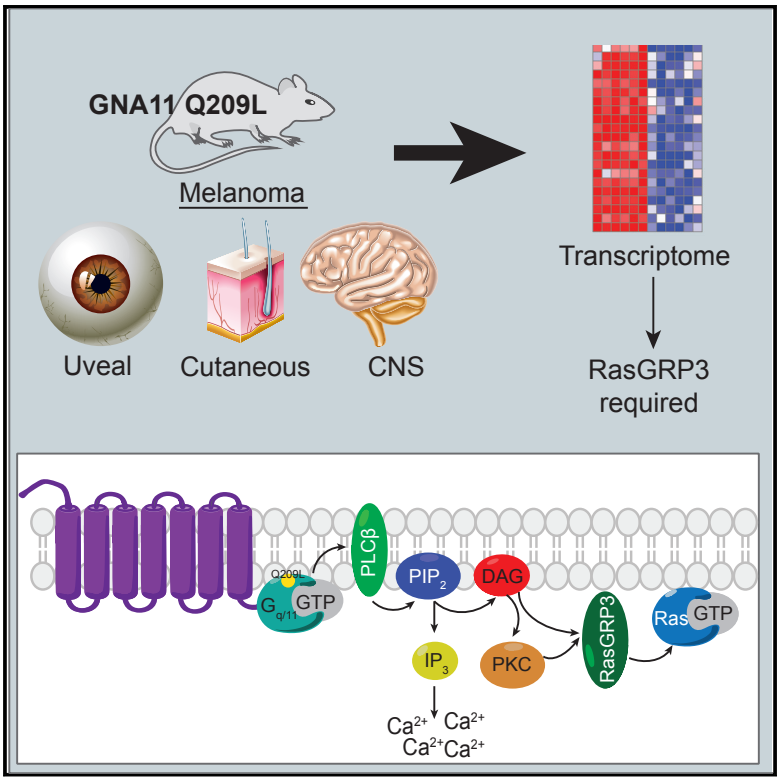

Authors

Amanda R. Moore, Leili Ran, Youxin Guan, ..., Klaus G. Griewank, Ping Chi, Yu Chen

Correspondence

chip@mskcc.org (P.C.), cheny1@mskcc.org (Y.C.)

In Brief

Moore et al. generate a preclinical mouse model of melanoma that recapitulates features of aggressive uveal melanoma. By comparing murine and human melanomas, they identify a dependency on RasGRP3 in uveal melanoma.

Highlights

- GNA11 Q209L mouse model induces uveal, cutaneous, and leptomeningeal melanoma
- Loss of Bap1 promotes aggressive melanomas
- RasGRP3 links GNA11/GNAQ activation to RAS activation
- RasGRP3 is required for GNA11/GNAQ-driven tumorigenesis

Data and Software Availability

GSE97225

Moore et al., 2018, Cell Reports 22, 2455–2468
February 27, 2018
https://doi.org/10.1016/j.celrep.2018.01.081

CellPress

Cell Reports
Article

GNA11 Q209L Mouse Model Reveals RasGRP3 as an Essential Signaling Node in Uveal Melanoma

Amanda R. Moore,[1,2] Leili Ran,[1,3] Youxin Guan,[1] Jessica J. Sher,[1] Tyler D. Hitchman,[1,3] Jenny Q. Zhang,[1] Catalina Hwang,[1] Edward G. Walzak,[1] Alexander N. Shoushtari,[4,5] Sébastien Monette,[6] Rajmohan Murali,[7,8] Thomas Wiesner,[9] Klaus G. Griewank,[10] Ping Chi,[1,4,5,*] and Yu Chen[1,4,5,11,*]

[1]Human Oncology and Pathogenesis Program, Memorial Sloan Kettering Cancer Center, 1275 York Avenue, New York, NY 10065, USA
[2]Weill Cornell Graduate School of Medical Sciences, Cornell University, 1300 York Avenue, New York, NY 10065, USA
[3]Gerstner Sloan Kettering Graduate School of Biomedical Sciences, Memorial Sloan Kettering Cancer Center, 1275 York Avenue, New York, NY 10065, USA
[4]Department of Medicine, Memorial Sloan Kettering Cancer Center, 1275 York Avenue, New York, NY 10065, USA
[5]Department of Medicine, Weill Cornell Medical College, 1300 York Avenue, New York, NY 10065, USA
[6]Laboratory of Comparative Pathology, Memorial Sloan Kettering Cancer Center, The Rockefeller University, Weill Cornell Medicine, 1275 York Avenue, New York, NY 10065, USA
[7]Department of Pathology, Memorial Sloan Kettering Cancer Center, 1275 York Avenue, New York, NY 10065, USA
[8]Marie-Josée and Henry R. Kravis Center for Molecular Oncology, Memorial Sloan Kettering Cancer Center 1275 York Avenue, New York, NY 10065, USA
[9]Department of Dermatology, Medical University of Vienna, Vienna, Austria
[10]Department of Dermatology, University Hospital Essen, West German Cancer Center, University Duisburg-Essen and the German Cancer Consortium, Essen, Germany
[11]Lead Contact
*Correspondence: chip@mskcc.org (P.C.), cheny1@mskcc.org (Y.C.)
https://doi.org/10.1016/j.celrep.2018.01.081

SUMMARY

Uveal melanoma (UM) is characterized by mutually exclusive activating mutations in *GNAQ*, *GNA11*, *CYSLTR2*, and *PLCB4*, four genes in a linear pathway to activation of PLCβ in almost all tumors and loss of BAP1 in the aggressive subset. We generated mice with melanocyte-specific expression of $GNA11^{Q209L}$ with and without homozygous Bap1 loss. The $GNA11^{Q209L}$ mice recapitulated human Gq-associated melanomas, and they developed pigmented neoplastic lesions from melanocytes of the skin and non-cutaneous organs, including the eye and leptomeninges, as well as at atypical sites, including the lymph nodes and lungs. The addition of Bap1 loss increased tumor proliferation and cutaneous melanoma size. Integrative transcriptome analysis of human and murine melanomas identified RasGRP3 to be specifically expressed in GNAQ/GNA11-driven melanomas. In human UM cell lines and murine models, RasGRP3 is specifically required for GNAQ/GNA11-driven Ras activation and tumorigenesis. This implicates RasGRP3 as a critical node and a potential target in UM.

INTRODUCTION

Uveal melanomas (UMs) arise from the melanocytes of the eye. While localized disease can be effectively treated surgically, half of all patients develop metastasis, and metastatic UM carries a dismal prognosis with an overall survival of only 6 months (Diener-West et al., 2005). Approximately half of the patients harbor metastases to multiple organs, with liver (93%), lung (24%), bone (16%), and lymph nodes (10%) representing the most common sites (Collaborative Ocular Melanoma Study Group, 2001). Over the past decade, we have gained considerable insight into the genetic basis of UM. This has not yet led to novel therapeutic options and there are still no proven systemic treatments for UM.

UM is highly distinct from cutaneous melanoma (CM) both clinically and molecularly. UM is not associated with sun exposure and has among the lowest mutation rates in cancer, whereas CM has among the highest mutation rates due to UV damage (Furney et al., 2013). A recent comparison of liver metastasis revealed that most CM metastases lacked gross melanin pigmentation while most UM metastases are hyperpigmented and express high levels of melanocyte lineage proteins, such as MART-1 (*MLANA*) and gp100 (*PMEL*) (Rothermel et al., 2016). Molecularly, CM is driven by recurrent somatic mutations that activate the mitogen-activated protein kinase (MAPK) pathway, including *BRAF*, *NRAS*, *NF1*, and *KIT*. Approximately 90% of UMs harbor activating mutations in two homologous G-protein alpha (Gα) subunits, *GNA11* ($G\alpha_{11}$) and *GNAQ* ($G\alpha_q$), at codons Gln209 or Arg183 (Robertson et al., 2017; Van Raamsdonk et al., 2009, 2010). Among the remaining 10% of UMs, most harbor activating mutations in a G-protein-coupled receptor (*CYSLTR2* at the Leu129 codon activates $G\alpha_{11/q}$) or in phospholipase C β4 (*PLCB4*) (at the Asp630 codon, a direct downstream effector of $G\alpha_{11/q}$ cleaves phosphatidylinositol 4,5-bisphosphate [PIP_2] to produce the second messengers diacylglycerol [DAG] and inositol triphosphate [IP_3] (Johansson et al., 2016; Moore et al., 2016). This indicates a requirement for $G\alpha_{11/q}$-coupled signaling and, in particular, the phospholipase Cβ (PLCβ) effector pathway in the initiation of UMs.

While essentially all UMs harbor mutations in the CYSLTR2-$G\alpha_{11/q}$-PLCβ pathway, the prognosis is largely determined by the presence of cooperative mutations. Monosomy 3 and an associated poor-prognosis gene expression pattern is the single most negative prognostic factor. Most of these tumors harbor inactivating mutations in *BAP1*, located at 3q21, and essentially all of these tumors lose expression of the BAP1 protein, implicating BAP1 loss as a critical cooperating lesion driving poor prognosis in UM (Harbour et al., 2010; Robertson et al., 2017). Among tumors with disomy 3, there are mutually exclusive mutations in *SF3B1*, associated with intermediate prognosis, and in *EIF1AX*, associated with favorable prognosis (Martin et al., 2013; Robertson et al., 2017).

In addition to UM, CYSLTR2-$G\alpha_{11/q}$-PLCβ pathway mutations are found in most leptomeningeal melanocytic neoplasms (LMNs) and blue nevi (Möller et al., 2017; Van Raamsdonk et al., 2009). LMNs are rare neoplasms arising from melanocytes of the leptomeninges. Like UM, in addition to mutations in *GNA11* and *GNAQ*, LMNs harbor mutually exclusive co-mutations in either *EIF1AX* or *SF3B1* in 33% of cases (Küsters-Vandevelde et al., 2016). Blue nevi are common benign neoplasms of dermal melanocytes, which are distinguished from CMs that arise from epidermal melanocytes. Rare malignant melanomas that either arise from blue nevi or show morphologic features of blue nevi are called malignant blue nevi. Recent genetic characterization of a large cohort of blue nevi showed both benign and malignant blue nevi harbored CYSLTR2-$G\alpha_{11/q}$-PLCβ pathway mutations (Möller et al., 2017). *EIF1AX* mutations are found only in benign blue nevi, while *SF3B1* and *BAP1* mutations are found only in malignant blue nevi (Griewank et al., 2017). Therefore, UM, LMN, and blue nevi represent a molecularly similar spectrum of diseases that commonly harbor CYSLTR2-$G\alpha_{11/q}$-PLCβ mutations and whose disease aggressiveness is defined by co-mutations, especially *BAP1.*

Because the PLCβ pathway is known to activate MAPK, the MEK inhibitor selumetinib has been clinically studied. While a phase 2 trial showed promising improvement in progression-free survival, the phase 3 trial failed to confirm the finding and neither trial showed an improvement in overall survival (Carvajal et al., 2014; Komatsubara et al., 2016). As different MEK inhibitors have distinct properties (Lito et al., 2014), it is still currently unclear whether the MAPK pathway remains a viable therapeutic target in UM.

To identify molecular and lineage events downstream of $G\alpha_{11}$ activation, the cooperative role of BAP1 loss, and critical nodes required for $G\alpha_{11}$-mediated tumorigenesis, we generated a conditional Rosa26-LSL-$GNA11^{Q209L}$ mouse model and crossed it with conditional Bap1 knockout (KO) mice. These mice recapitulate the features of human $G\alpha_{11}$-driven melanomas. They developed neoplastic hyperpigmented melanocytic lesions in the uveal tract, skin, and leptomeninges. These mice developed lesions in the lung and lymph nodes. Deletion of *Bap1* accelerated skin tumor growth and mouse mortality. The $GNA11^{Q209L}$, Bap1 loss tumors were resistant to the MEK inhibitor trametinib. To identify alternative therapeutic targets, we performed integrative analysis comparing BRAF mutant and $G\alpha_{11/q}$ mutant human and murine cancers, and we identified a critical requirement of a Ras guanine exchange factor (GEF), RasGRP3, for $G\alpha_{11/q}$-mediated tumorigenesis.

RESULTS

Melanocyte-Specific *GNA11*^{Q209L} Expression Induces Skin, Uveal, and CNS Neoplasia

To express $GNA11^{Q209L}$ in the melanocyte lineage, we generated a genetically engineered mouse model (GEMM) with a conditional $GNA11^{Q209L}$ allele (*R26-LSL-*$GNA11^{Q209L}$) under the control of the endogenous *Rosa26* promoter (Figures S1A and S1B). To identify an active Cre-driver for uveal melanocytes, we crossed *Tyr-*$CreER^{T2}$ transgenic mice that express tamoxifen-inducible $CreER^{T2}$ under the melanocyte-specific *Tyrosinase* (*Tyr*) promoter with the CAG-LSL-EYFP reporter. One week after tamoxifen injection, there was robust EYFP expression in both uveal and skin (hair follicle) melanocytes (Figure S1C). We thus generated *Tyr-*$CreER^{T2}$*;*$GNA11^{Q209L}$ mice for our studies.

To activate $GNA11^{Q209L}$ expression, we treated 4-week-old mice with a single application of tamoxifen or vehicle by intraperitoneal injection. In tamoxifen-injected, but not vehicle-injected, mice, we observed hyperpigmentation of ears and tail within 2 weeks of treatment and bulging eyes within 1 month of treatment (Figure S2A). In vehicle-treated *Tyr-*$CreER^{T2}$-positive or tamoxifen-treated *Tyr-*$CreER^{T2}$-negative control mice, there was no discernible pathologic phenotype in the skin or the uveal tract up to 18 months (Figures 1A, 1B, S2B, and S2C). In *Tyr-*$CreER^{T2}$*;*$GNA11^{Q209L}$ mice, pathological analysis of the skin 3 months post-induction showed extensive follicular and dermal melanocytic proliferation (Figure 1C), which progressed to melanomas encompassing the dermis and subcutaneous tissues in 50% of mice by 6 months after injection (Figure 1D). These proliferating melanocytes stained positive for a melanocyte cocktail (Figure S2D). Tumor cells contained abundant pale amphophilic cytoplasm and a small nuclear-to-cytoplasmic ratio (Figure S2D). For comparison, we also treated *Tyr-*$CreER^{T2}$*;*$BRaf^{CA/+}$ mice, which express the conditional $BRaf^{V600E}$ allele in melanocytes. We observed melanocytic hyperplasia without progression to melanoma up to 12 months post-induction, similar to previous observations (Figure S2E) (Dankort et al., 2009).

We next examined the oncogenic role of $GNA11^{Q209L}$ and $BRaf^{V600E}$ expression in uveal melanocytes. Within the uveal tract, tamoxifen-injected *Tyr-*$CreER^{T2}$*;*$GNA11^{Q209L}$ mice displayed diffuse hyperplasia, thickening of the choroid and ciliary body that progressed over time to overt UM with intraocular infiltration that distorted the normal architecture of the globe (Figures 1E and 1F). Uveal melanocyte proliferation was evident in mice as early 1 month post-tamoxifen (data not shown). In contrast, the uveal tracts of induced *Tyr-*$CreER^{T2}$*;*$BRaf^{CA/+}$ mice were indistinguishable from those of control mice (Figures S2F and S2G). Further examination revealed tumor cells with pathological characteristics similar to skin melanoma (Figure 1G, i and ii). These cells were positive for MITF and melanocyte cocktail staining (Figure 1G, iii and iv). We further observed perineural spread of malignant melanoma to the optic nerve (Figure 1H).

We next examined the effect of *GNA11*^{Q209L} in resident melanocytes of other organs, including the heart, harderian gland,

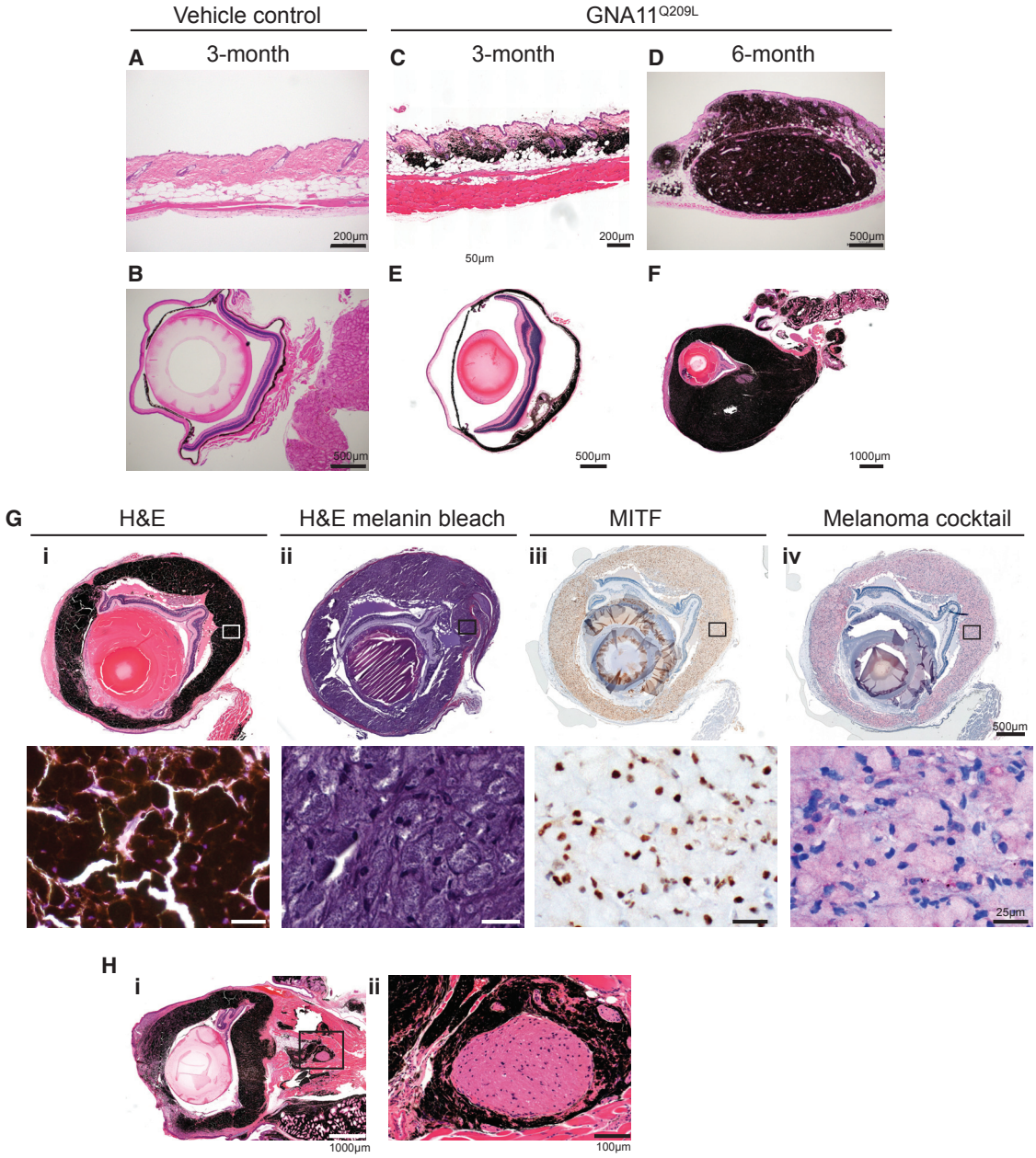

Figure 1. Melanocyte-Specific *GNA11*^{Q209L} Expression Induces Cutaneous and UM

(A and B) H&E of skin (A) and eye (B) from *Tyr-CreER*^{T2}-negative control mice 3 months post-induction.

(C and D) H&E of skin from GNA11^{Q209L} mice 3 months (C) or 6 months (D) post-induction.

(E and F) H&E of eyes from GNA11^{Q209L} mice 3 months (E) or 6 months (F) post-induction.

(G) H&E (i), H&E with melanin bleaching (ii), MITF immunohistochemistry (IHC) using diaminobenzidine (DAB) (brown) (iii), and melanoma cocktail IHC using red chromogen (red) (iv) from a GNA11^{Q209L} mouse 6 months post-induction. High-magnification insets of top panels are shown in bottom panel.

(H) H&E of a selected eye (i) with melanocytic perineural invasion of the optic nerve (ii).

See also Figures S1 and S2.

and brain (Aoki et al., 2009). Gross examination of the brain revealed focal pigmentation of the leptomeninges in 80% of mice (Figure S3A). Pathological evaluation of the CNS of the *Tyr-CreER*^{T2}*;GNA11*^{Q209L} mice showed melanocytic proliferation in the leptomeninges at the base of the brain, around cranial nerve roots, and within the longitudinal fissure (Figure 2A, ii–iv). There was prominent melanocytic hyperplasia within the third ventricle (Figure 2A, i and iv). Clinically, primary melanocytomas occasionally occur within the ventricular system of the CNS (Tandon et al., 2008). There was invasion of melanocytes to the

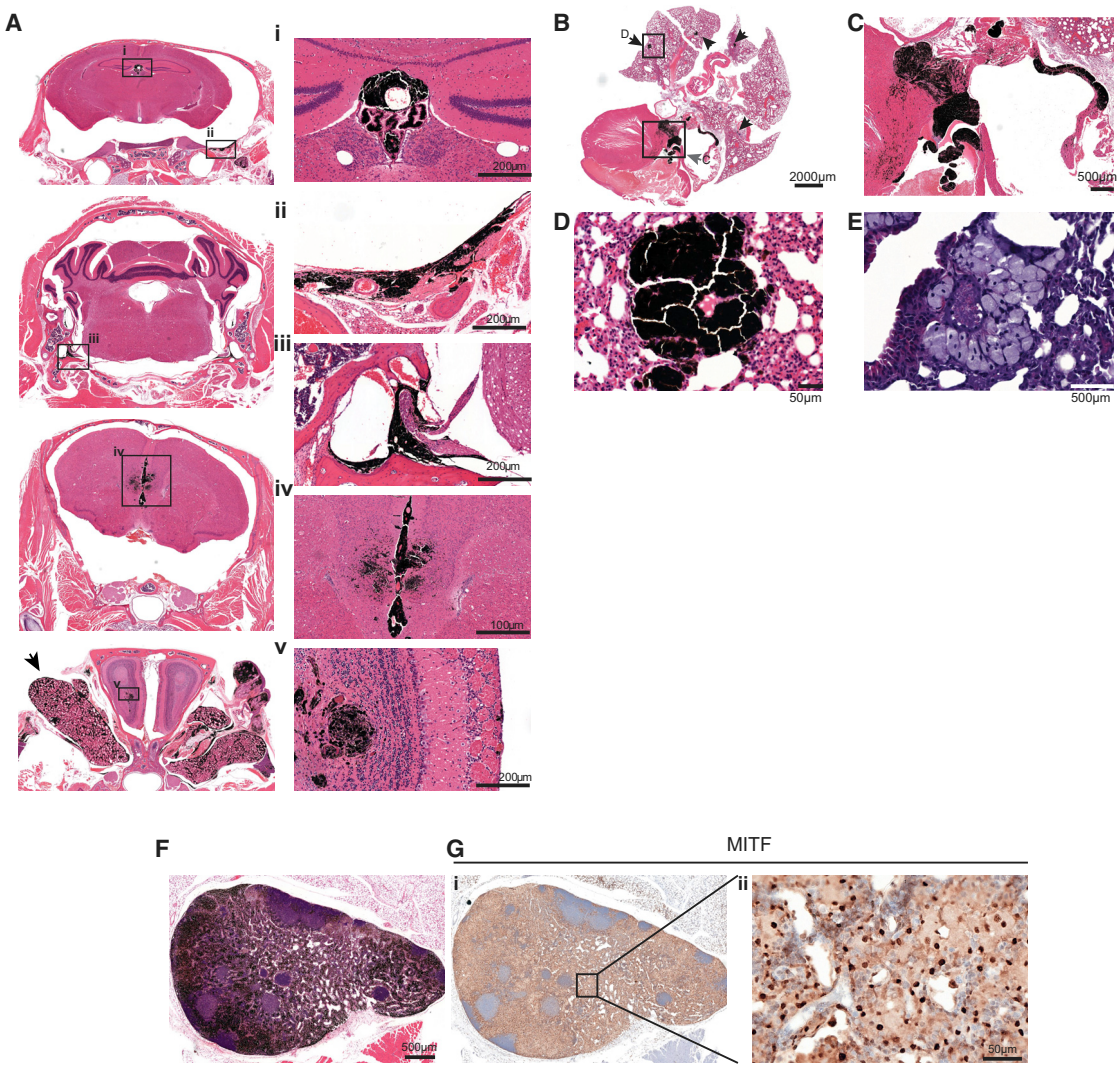

Figure 2. Melanocyte-Specific *GNA11*^{Q209L} Expression Induces Leptomeningeal Melanocytic Neoplasia and Possible Metastasis

(A) H&E of coronal skull sections (left), magnified images of regions showing melanocytic neoplasia in the (i) choroid plexus of the third ventricle (i), leptomeninges of brain base surrounding cranial nerve roots (ii and iii), longitudinal fissure and ependyma of the third ventricle olfactory bulb (iv and v). Arrow indicates the harderian gland.

(B) H&E of heart and lung. Arrows indicate lesions.

(C) Magnification of heart in (B) showing melanoma in the tricuspid valve, right atrial wall, and interventricular septum indicated by box and gray arrow in (B).

(D and E) Magnification of a selected melanocytic lesion (D) in the lung indicated by box and arrow in (B) and with melanin bleaching (E).

(F and G) H&E (F) and MITF IHC (G) of axillary lymph node melanocytic lesion (G, ii).

See also Figure S3.

periventricular space, and one mouse exhibited invasion to the olfactory bulb (Figure 2A, iv and v). We observed robust proliferation of resident melanocytes in the harderian gland (Figure 2A, arrow).

Examining the melanocytes of the heart in GNA11^{Q209L} mice, we observed invasive neoplasms that infiltrated and thickened the tricuspid valve and infiltrated the myocardium of the right atrium and interventricular septum (Figures 2B and 2C). We suspect these lesions were primary tumors of the resident melanocytes of the heart. Melanocytic lesions were not evident in *Tyr-CreER*^{T2}*;BRaf*$^{CA/+}$ mice in these areas (Figures S3C and S3D).

In GNA11^{Q209L} mice, we observed multi-focal lesions in the lungs that may represent metastases, although we cannot rule out transformation of rare resident lung melanocytes (Figures 2B, 2D, and 2E). However, the morphology of these lesions resembled the primary tumors (Figures 1D, 1G, ii, 2B, and 2C). These lesions occurred early and were observed in mice with less advanced skin and uveal lesions (Figure S3E). We observed melanocytes infiltrating the lymphatic system, as visualized by MITF staining in the axillary lymph nodes (Figures 2F and 2G). In contrast, we did not observe melanocytic lesions in the CNS, heart, lungs, or lymph nodes in *Tyr-CreER*^{T2}*;BRaf*$^{CA/+}$

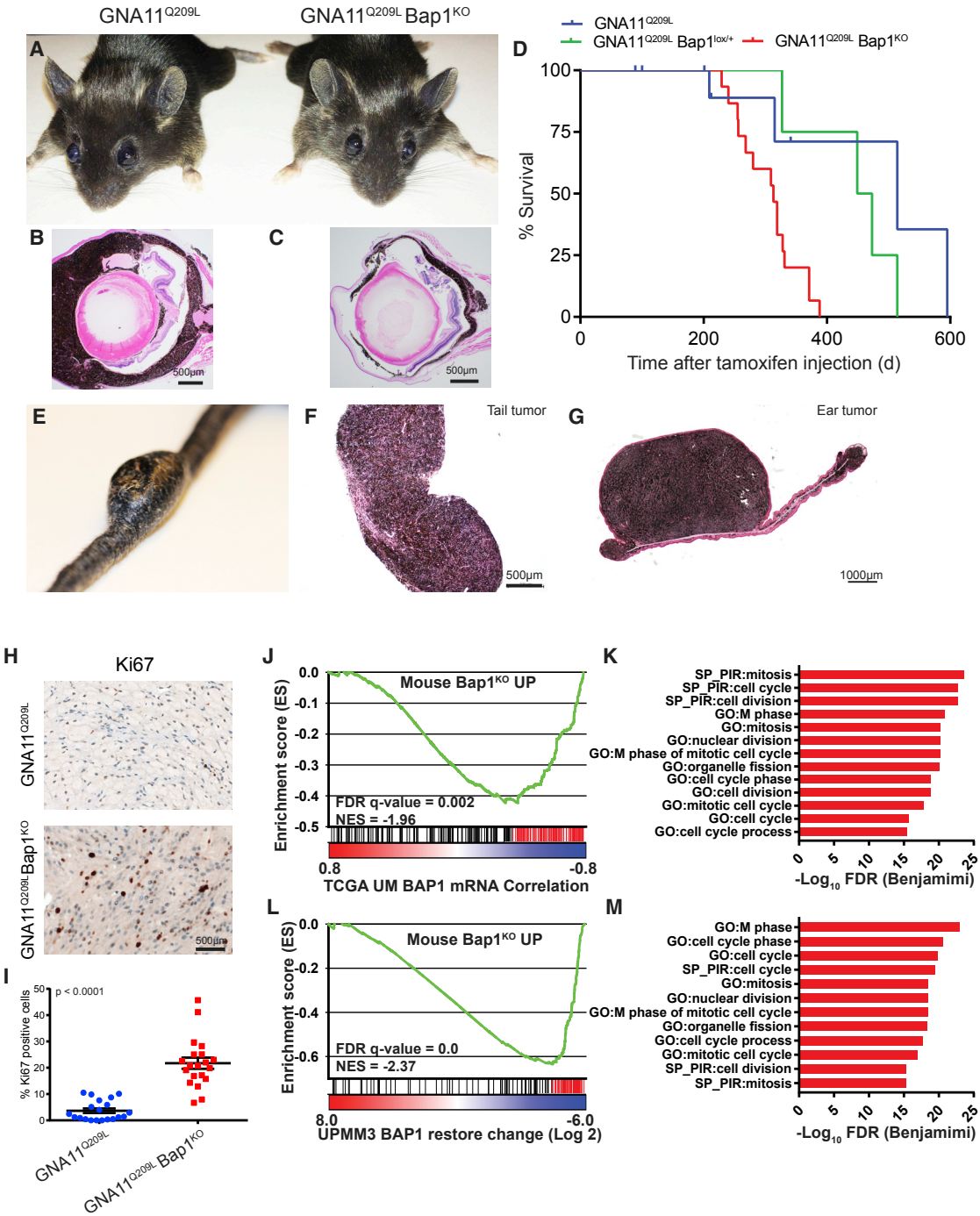

Figure 3. Bap1 Loss Promotes Aggressive Melanomas

(A) Photographs of GNA11^{Q209L} (left) and GNA11^{Q209L} Bap1^{KO} (right) mice 3 months post-induction.

(B and C) H&E of eyes from GNA11^{Q209L} (B) and GNA11^{Q209L} Bap1^{KO} (C) mice 12 months post-induction.

(D) Kaplan-Meier curve comparing the survival percentage of GNA11^{Q209L} (blue) or GNA11^{Q209L} Bap1$^{lox/+}$ (green) to GNA11^{Q209L} Bap1^{KO} mice (red). p = 0.0013.

(E and F) Photograph of large invasive melanoma from the tail dermis (E) and H&E (F) from a GNA11^{Q209L} Bap1^{KO} mouse 12 months post-induction.

(G) H&E of an invasive melanoma from the dermis of the ear from a GNA11^{Q209L} Bap1^{KO} mouse 12 months post-induction.

(H) Ki-67 IHC in GNA11^{Q209L} (top) and GNA11^{Q209L} Bap1^{KO} (bottom) cutaneous tumors.

(I) Quantification of Ki-67-positive cells. Scatter-dot plot: each dot represents the quantification of one field. Error bars represent means ± SEM. p < 0.0001.

(J) GSEA plot using a gene set comprised of genes upregulated in mice (Mouse_Bap1KO_UP) on a profile of genes ranked by correlation to *BAP1* expression in the UM TCGA dataset.

(legend continued on next page)

mice (Figures S3B–S3D). Our data are consistent with the clinical absence of *BRAF* mutations in UMs and LMNs and the sporadic occurrence of *GNAQ/11* mutations in CMs.

Recently, a mouse model harboring GNAQ^{Q209L} was characterized (Huang et al., 2015). When activated in melanoblasts during embryogenesis with *Mitf-Cre*, the mice exhibited UM, LMN, neoplastic melanocytic growth in the harderian glands, and rare lesions in the skin, as well as lymph nodes and lung (Huang et al., 2015). When activated in 8-week-old adult mice using *Tyr-CreER^{T2}*, GNAQ^{Q209L} drove melanocyte overgrowth without progression to melanoma. The phenotype of our *Tyr-CreER^{T2};GNA11^{Q209L}* mouse model, activated at 4 weeks, appears to be an intermediate between *Mitf-Cre* activated before birth and *Tyr-CreER^{T2}* activated at 8 weeks. The *Mitf-Cre;GNAQ^{Q209L}* mice developed earlier invasive UM and more diffuse LMN, likely due to earlier expression at mid-gestation and prolonged Cre activation (Alizadeh et al., 2008).

Loss of *Bap1* Accelerates Skin Melanomas in the Presence of GNA11^{Q209L}

We sought to examine the combinatorial effect of GNA11^{Q209L} and the loss of the tumor suppressor Bap1 in the development of UM. To achieve *Bap1* deletion, we crossed *Bap1$^{lox/lox}$* mice (LaFave et al., 2015) to the *Tyr-CreER^{T2};GNA11^{Q209L}* line. Tamoxifen-treated *Tyr-CreER^{T2};Bap1^{KO}* mice had no discernible phenotype and were histologically normal over ~20 months, indicating Bap1 loss alone was insufficient to initiate melanoma (n = 35; Figures S4A and S4B).

We compared the *Tyr-CreER^{T2};GNA11^{Q209L};Bap1$^{lox/lox}$* mice to the *Tyr-CreER^{T2};GNA11^{Q209L}* mice. We observed a stronger ocular phenotype in *GNA11^{Q209L}* than *GNA11^{Q209L} Bap1^{KO}* mice (Figures 3A–3C). However, the *GNA11^{Q209L} Bap1^{KO}* mice succumbed to disease at an accelerated rate compared to *GNA11^{Q209L}* or *GNA11^{Q209L} Bap1$^{lox/+}$* mice (Figure 3D; $p < 0.05$), due to increased skin melanoma burden (Figures 3E and 3F). The loss of Bap1 in these mice did not appreciably alter the size or incidence of uveal lesions, but it contributed to an increased progression to skin melanomas originating from the tail and ears (Figures 3E–3G). We confirmed Bap1 KO in uveal melanocytes using PCR (Figure S4C). Unlike in human UM patients, no pigmented liver lesions were observed (Figures S4D and S4E). We observed no significant increase in the size or incidence of lung lesions in the absence of Bap1 (Figures S3E and S4F–S4H). Histologically, GNA11^{Q209L} skin melanomas exhibited slender oval nuclei while GNA11^{Q209L};Bap1^{KO} had larger euchromatic nuclei (Figure 3H). GNA11^{Q209L};Bap1^{KO} skin melanomas exhibited a higher proliferation index (Figures 3H and 3I; $p < 0.0001$).

To determine the extent that Bap1 KO molecularly recapitulates human melanoma and to understand the Bap1-regulated transcriptional programs, we performed transcriptome analysis of mouse and human melanomas. RNA sequencing (RNA-seq) revealed the *R26-GNA11^{Q209L}* transcript level was 4- to 8-fold lower than endogenous murine *Gnaq* and *Gna11* transcript levels, indicating modest expression of mutant *GNA11* is required for tumorigenesis (Figure S5A). Analysis of RNA-seq of GNA11^{Q209L} and GNA11^{Q209L};Bap1^{KO} skin melanomas confirmed deletion of *Bap1* (Figure S5B). Using a gene set comprised of genes upregulated in GNA11^{Q209L};Bap1^{KO} versus GNA11^{Q209L} skin melanomas (Mouse_Bap1KO_UP), we performed gene set enrichment analysis (GSEA) using The Cancer Genome Atlas (TCGA) UM dataset (Robertson et al., 2017). This showed Mouse_Bap1KO_UP genes are significantly enriched among genes negatively correlated with *BAP1* expression in UM, suggesting BAP1 deletion in skin melanomas of mice results in the upregulation of similar genes to human UM (Figure 3J; Table S1). To explore the function of the shared genes, we performed functional annotation of the leading edge genes (Figure 3J, red) that drove the GSEA enrichment. We found the most enriched gene ontology (GO) and Swiss-Prot (SP) pathways all involved cell cycle and mitosis (Figure 3K).

In a complementary approach, we identified a UM primary tumor line, UPMM3, contained a frameshift deletion of *BAP1* (Figure S5C) (Griewank et al., 2012). We restored wild-type BAP1 (Figure S5D) and generated a gene expression profile using RNA-seq. As controls, we expressed BAP1 with mutations in the deubiquitinase domain (p.Cys91Trp, p.Ala95Pro) found in cancer (Harbour et al., 2010) as well as EGFP. Wild-type BAP1 restoration significantly changed gene expression while the presumably non-functional mutants did not, observed by gene hierarchical clustering (Figure S5E). We next performed GSEA, and we found the Mouse_Bap1KO_UP gene set was significantly enriched among genes downregulated in UPMM3 cells by BAP1 (wild-type [WT]) restoration (Figure 3L). Functional analysis of leading edge genes showed cell cycle pathways were enriched (Figure 3M). GSEA on three BAP1 datasets (mouse model, TCGA, and UPMM3) using the >8,300 gene sets from the Molecular Signatures Database (MSigDB) showed cell cycle and melanoma metastasis signatures are highly enriched in each (Table S1; Figures S5F and S5G). Therefore, in UM, the loss of Bap1 can promote aggressive disease with a propensity to proliferate and metastasize, consistent with clinical data implicating BAP1 loss as a poor prognostic biomarker.

G$\alpha_{11/q}$-Driven Cells Have Reduced Sensitivity to MEK Inhibition

Activation of the G$\alpha_{11/q}$-PLCβ pathway leads to downstream activation of the MAPK pathway. While preclinical data using UM cell lines suggest MEK inhibition may be a therapeutic strategy (Ambrosini et al., 2012), a recent phase 3 study comparing selumetinib and chemotherapy failed to show significant improvement in progression-free or overall survival (Komatsubara et al., 2016).

(K) GO and SP pathways from leading edge genes (red; J) upregulated in GNA11^{Q209L} Bap1^{KO} tumors and negatively correlated with *BAP1* expression in TCGA UM.

(L) GSEA plot using Mouse_Bap1KO_UP gene set (as in J) on a profile of genes ranked by change in UMMP3 cells upon BAP1 wild-type (WT) restoration.

(M) GO and SP pathways from leading edge genes (red; L) upregulated in GNA11^{Q209L} Bap1^{KO} tumors and downregulated upon BAP1 restoration in UMMP3 cells.

See also Figures S4 and S5 and Table S1.

Prolonged selumetinib treatment induces RAF-MEK dimer formation, leading to reactivation of MAPK signaling, particularly in non-BRAF^{V600E}-driven tumors. The newer MEK inhibitor trametinib uniquely decreases RAF-MEK interaction and MAPK reactivation (Lito et al., 2014).

To address whether improved MEK inhibition can lead to therapeutic efficacy in UM, we utilized the GEMMs to perform *in vivo* trametinib treatment. We needed relevant control tumors that formed nodules of a similar size and were responsive to trametinib treatment. We observed Bap1^{KO} also accelerated BRaf^{V600E}-driven tumors to form nodules amenable for treatment (unpublished data). We subcutaneously grafted skin melanomas, isolated from *BRaf^{V600E};Bap1^{KO}* and *GNA11^{Q209L};Bap1^{KO}* mice, into severe combined immunodeficiency (SCID) mice. The grafts retained features of the *in situ* tumors, where GNA11^{Q209L};Bap1^{KO} tumors retained hyperpigmentation whereas BRaf^{V600E};Bap1^{KO} tumors were hypopigmented and exhibited elevated MAPK output (Figures 4A and 4B). In BRaf^{V600E} Bap1^{KO} tumors, short-term trametinib treatment decreased proliferation and MAPK output, whereas in GNA11^{Q209L} Bap1^{KO} tumors, the effects were modest (Figures 4A–4C). Long-term treatment resulted in initial tumor shrinkage followed by stabilization in BRaf^{V600E} Bap1^{KO} tumors (Figure 4D). However, GNA11^{Q209L} Bap1^{KO} tumors were resistant to trametinib treatment (Figure 4D). To determine if relative resistance to trametinib treatment was more generalized, we treated human BRAF^{V600E} CM and G$\alpha_{q/11}$ mutant UM cell lines with a clinically achievable concentration of trametinib (10 nM) (Infante et al., 2012). Trametinib sustainably inhibited MAPK in CM cells. In UM cells, MEK phosphorylation was stable or increased over time and ERK phosphorylation was variably inhibited but rebounded by 24 hr (Figure 4E). This is consistent with known hypersensitivity of BRAF^{V600E} melanoma to MEK inhibition (Solit et al., 2006). Together, activating mutations in the G$\alpha_{11/q}$ pathway exhibit *in vivo* and *in vitro* resistance to MEK inhibition. This highlights the need for novel therapeutic targets in UM.

Cross-Species Analysis Shows G$\alpha_{11/q}$-Driven Tumors Enforce a Melanocyte Lineage Program and Express High Levels of RASGRP3

To identify critical nodes in G$\alpha_{11/q}$-mediated tumorigenesis, we utilized a cross-species transcriptome analysis approach of human and murine melanoma. We sought to generate a transcriptional signature of Gα_{11}-driven GEMM melanoma. We generated GEMM Gα_{11} and BRaf signatures with differentially expressed genes between GNA11^{Q209L} Bap1^{KO} and BRaf^{V600E} Bap1^{KO} melanomas (>3-fold, false discovery rate [FDR] < 0.01). In human melanoma, we combined and curated TCGA skin CM (SKCM) (Cancer Genome Atlas, 2015) and UM datasets, and we compared tumors with hotspot mutations in G$\alpha_{11/q}$ (74/80 UM and 5/333 SKCM) with BRAF^{V600E} (0/80 UM and 121/333 SKCM). GSEA using the GEMM signatures on the TCGA transcriptomes showed significant enrichment of the Gα_{11} and Braf signatures in human G$\alpha_{11/q}$-mutated and BRAF^{V600E} tumors, respectively (Figure 5A). Therefore, the oncogenic signaling driver, in addition to the location of the tumor, contributes to the oncogenic transcriptome. Functional annotation of the leading edge G$\alpha_{11/q}$ signature genes showed upregulation of pigmentation and melanocyte differentiation pathways (Figures 5B–5D), consistent with the observation of highly pigmented melanomas in the GNA11^{Q209L} GEMM (Figures 1, 2, and 4). This is also consistent with the clinicopathological observations that metastatic UMs retain greater pigmentation than CMs (Rothermel et al., 2016) and with our previous observation that *CYSLTR2^{L129Q}* enforces a melanocyte lineage (Moore et al., 2016).

Further examination of top-ranked genes identified *RASGRP3* as highly expressed in both G$\alpha_{11/q}$-mutated human and GEMM melanomas (Figures 5E and 5F). Pan-cancer analysis of RNA-seq datasets from TCGA (Figure 5E) and Affymetrix U133Plus2 datasets curated by gene expression across normal and tumor tissue (GENT) (Figure S6) showed *RASGRP3* is expressed at significantly higher levels in UMs than in CMs and other cancer types. Notably, all TCGA UMs expressed high *RASGRP3*, and the five TCGA SKCMs with the highest *RASGRP3* expression harbored either *GNAQ* or *GNA11* mutations and either BAP1 loss (mutation or monosomy 3) or *SF3B1* mutations, suggesting they may be malignant blue nevi (Griewank et al., 2017) (Figure 5E, circled). *RASGRP3* encodes Ras guanyl-releasing protein 3 (RasGRP3), a GEF that promotes the release of GDP-bound Ras in order to bind GTP, yielding active Ras (Ras-GTP) (Rebhun et al., 2000). RasGRP3 activation is dependent on both DAG binding and phosphorylation on Thr 133 by protein kinase C (PKC) (Aiba et al., 2004; Zheng et al., 2005). Together, these signaling events place the activation of RasGRP3 downstream of UM-activating mutations (*CYSLTR2*, *GNAQ*, *GNA11*, and *PLCB4*), and they suggest RasGRP3 may be a key signaling node that can integrate the UM-activating mutations into the MAPK pathway.

To determine if RasGRP3 expression is retained in cell lines, we screened a panel of UM and CM cells, and we found RasGRP3 to be expressed exclusively in UM cells (Figure 5G).

RasGRP3 Is Required for Ras-MAPK Activation and Growth in UM Cells

To determine if RasGRP3 is required for G$\alpha_{11/q}$-mediated activation of the MAPK pathway and for growth in UM, we generated two short hairpin RNAs (shRNAs) to mediate knockdown of *RASGRP3* (shRasGRP3-1 and shRasGRP3-2) and a control (shSCR). Depletion of RasGRP3 significantly reduced cell proliferation in *GNA11* or *GNAQ* mutant cells (Figures 6A and S7A). In contrast, knockdown of RasGRP3 in CM cells did not (Figures 6B and S7A).

We next sought to characterize the response of RasGRP3 depletion in the context of Ras activation and subsequent downstream MAPK signaling. We stably expressed two doxycycline (dox)-inducible RasGRP3 shRNAs (dox-shRasGRP3-1 and dox-shRasGRP3-2) and a dox-inducible control (dox-shSCR) in the panel of UM and CM cells. Depletion of RasGRP3 with dox significantly reduced the proportion of Ras-GTP and phosphorylation of ERK1/2 and P90^{RSK} in UM cells (Figure 6C). Consistent with the cellular growth data, there was no change in Ras activation or MAPK signaling upon depletion of RasGRP3 in CM cells (Figure 6C).

To elucidate the requirement of the Ras GEF activity of RasGRP3, we examined if ectopic expression of KRAS^{G12V} could rescue the proliferation and MAPK signaling in three UM cell lines depleted of RasGRP3. We performed growth

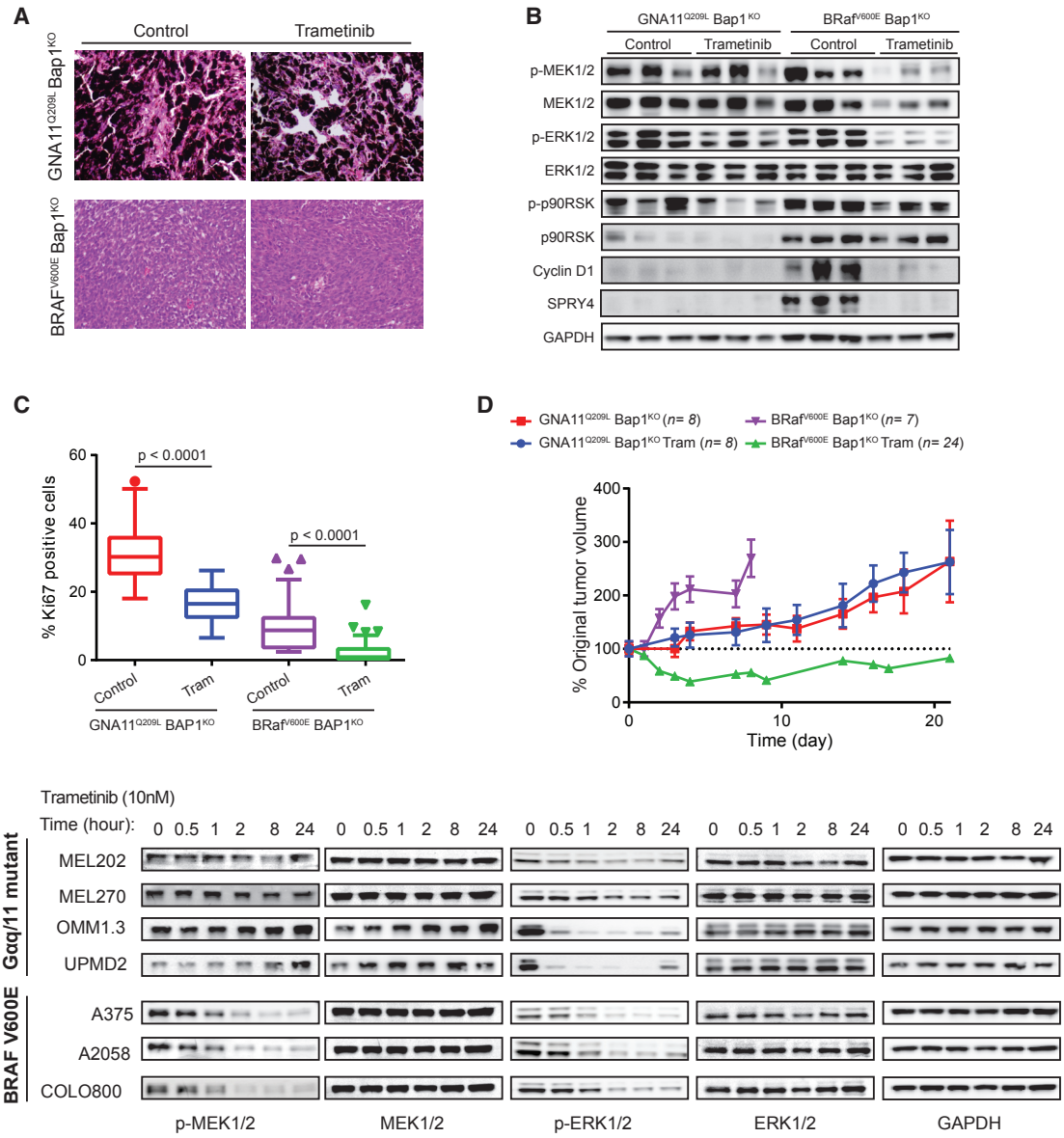

Figure 4. Reduced MEK Sensitivity in $G\alpha_{11/q}$-Driven Tumors

(A) H&E and Ki-67 IHC of GNA11^{Q209L} Bap1^{KO} and BRAF^{V600E} Bap1^{KO} tumors treated with trametinib or vehicle.

(B) Immunoblots for MAPK in explanted control and trametinib-treated GNA11^{Q209L} Bap1^{KO} and BRAF^{V600E} Bap1^{KO} tumors.

(C) Quantification of Ki67 in explanted control and trametinib-treated GNA11^{Q209L} Bap1^{KO} and BRAF^{V600E} Bap1^{KO} tumors, shown as Tukey box-and-whisker plots. Outliers are shown as dots. $p < 0.0001$.

(D) Tumor growth of grafted GNA11^{Q209L}Bap1^{KO} or BRAF^{V600E} Bap1^{KO} tumors in SCID mice with treatment as indicated. n = tumors per group. Error bars, SEM. $p < 0.001$ for BRAF^{V600E} Bap1^{KO} treatment.

(E) Immunoblot of $G\alpha_{11/q}$ mutant UM and BRAF mutant CM cell lines treated with 10 nM trametinib.

competition assays in which we first generated cells where 20%–50% expressed KRAS^{G12V}-IRES-GFP and empty vector at low MOI. We next infected these cells with shSCR or shRasGRP3, and we tracked the percentage of GFP-positive cells over time using fluorescence-activated cell sorting (FACS). The percentage of empty vector-expressing GFP-positive cells remained stable over time regardless of RasGRP3 depletion in both CM and UM cells (Figure S7B). In contrast, the percentage of KRAS^{G12V}-expressing GFP-positive cells increased after RasGRP3 depletion compared to shSCR in all three UM lines (Figure 6D), indicating KRAS^{G12V} conveys a growth advantage specifically after RasGRP3 depletion. Expression of KRAS^{G12V} rescued the reduction in ERK phosphorylation observed upon depletion of RasGRP3 (Figure 6E). Ectopic expression of KRAS^{G12V} in a CM cell line (A375) provided no changes in proliferation or ERK phosphorylation (Figures 6D

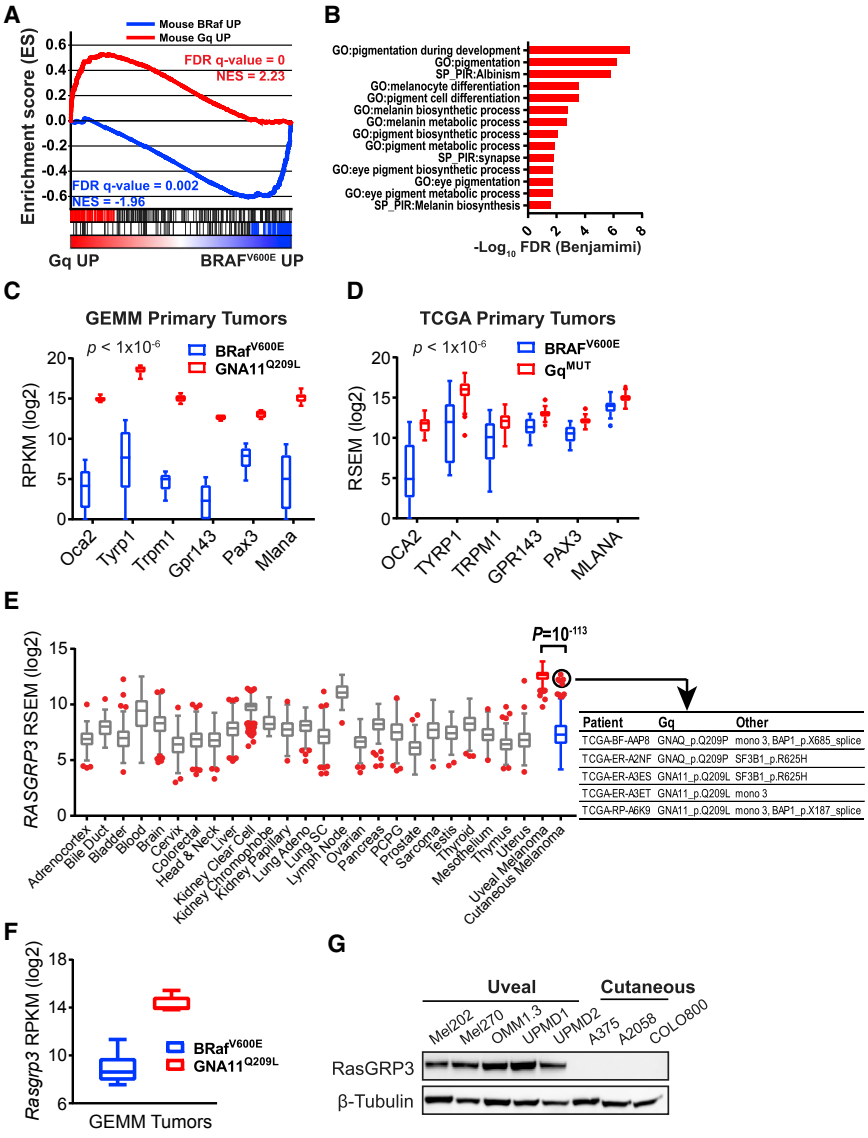

Figure 5. Gα$_{11/q}$-Driven Tumors Enforce a Melanocyte Lineage Program and Express High Levels of *RASGRP3*

(A) GSEA profile using the GEMM gene sets (Mouse BRaf UP and Mouse Gα$_{11/q}$ UP) on a profile ranked by expression difference between Gα$_{11/q}$ mutant and BRAF^{V600E} mutant melanomas in the combined TCGA SKCM and UM datasets.

(B) GO and SP pathways from leading edge genes (left; red; A) overexpressed in Gα$_{11/q}$ GEMM tumors and human Gα$_{11/q}$ mutant.

(C and D) Melanocyte-lineage genes shown as Tukey box-and-whisker plots from BRaf^{V600E} and GNA11^{Q209L} GEMM (C) and TCGA SKCM melanomas (D). Outliers are shown as dots. $p < 10^{-6}$.

(E) *RASGRP3* expression from pan-cancer TCGA shown as Tukey box-and-whisker plots. Outliers are shown as red dots. UM is highlighted in red. SKCM is highlighted in blue. Outliers with *GNAQ*, *GNA11*, *BAP1*, and *SF3B1* mutations are circled and detailed.

(F) RasGRP3 expression shown as Tukey box-and-whisker plots from GEMM tumors. $p < 10^{-6}$.

(G) Immunoblot of RASGRP3 in human UM and CM cell lines.

See also Figure S6.

and 6E). Therefore, UM cells require RasGRP3 for Ras activation and cellular proliferation.

RasGRP3 Is Required for Gα$_{11/q}$-Mediated Growth

Human UM cells harboring Gα$_{11/q}$ mutations selectively require RasGRP3 for growth and MAPK activation, suggesting Gα$_{11/q}$-mediated oncogenesis might require RasGRP3. To explore this hypothesis, we determined the requirement of RasGRP3 in an immortalized mouse melanocytic cell line, melan-a. Melan-a cells require phorbol esters, such as the DAG analog TPA (12-O-tetradecanoylphorbol-13-acetate), that can activate PKC for growth, and they can become TPA independent upon the expression of oncogenic mutations (Wellbrock et al., 2004). We transduced melan-a cells with GNAQ^{Q209L}, BRAF^{V600E}, and KRAS^{G12V}, and we cultured the cells in the absence of TPA to establish oncogene-dependent growth. At baseline, melan-a cells with TPA-dependent growth expressed endogenous Rasgrp3. While GNAQ^{Q209L}-dependent cells retained Rasgrp3, BRAF^{V600E}- and KRAS^{G12V}-dependent cells lost Rasgrp3 (Figure S7C). BRAF^{V600E}- and KRAS^{G12V}-dependent cells lost pigmentation and expression of melanocyte lineage proteins, while GNAQ^{Q209L}-dependent cells retained pigmentation and melanocyte lineage proteins (Figure S7C). Re-introduction of TPA to the media of BRAF^{V600E}- and KRAS^{G12V}-dependent cells failed to re-establish Rasgrp3 expression (Figure S7D). The difference in melanocyte lineage commitment between Gα$_{11/q}$ and RAS/RAF-driven transformed melanocytes is consistent with observations in our GEMMs and patient tumors.

To determine the potential role of RasGRP3 in Gα$_{11/q}$-, BRAF-, and KRAS-mediated tumorigenesis, we performed shRNA-mediated knockdown of *Rasgrp3* (shRasgrp3-1 and shRasgrp3-2). Knockdown of Rasgrp3 significantly reduced cell growth in GNAQ^{Q209L}-dependent, but not in BRAF^{V600E}- or KRAS^{G12V}-dependent, melan-a cells (Figures 7A and S7E). Depletion of Rasgrp3 in GNAQ^{Q209L} melan-a cells reduced Ras-GTP and the phosphorylation of ERK and P90^{RSK} (Figure 7B). Therefore, RasGRP3 is specifically required for Gα$_{11/q}$-mediated oncogenic growth.

DISCUSSION

UMs, LMNs, and blue nevi harbor activating mutations along the CYSLTR2-Gα$_{11/q}$-PLCβ pathway, and they can have mutually

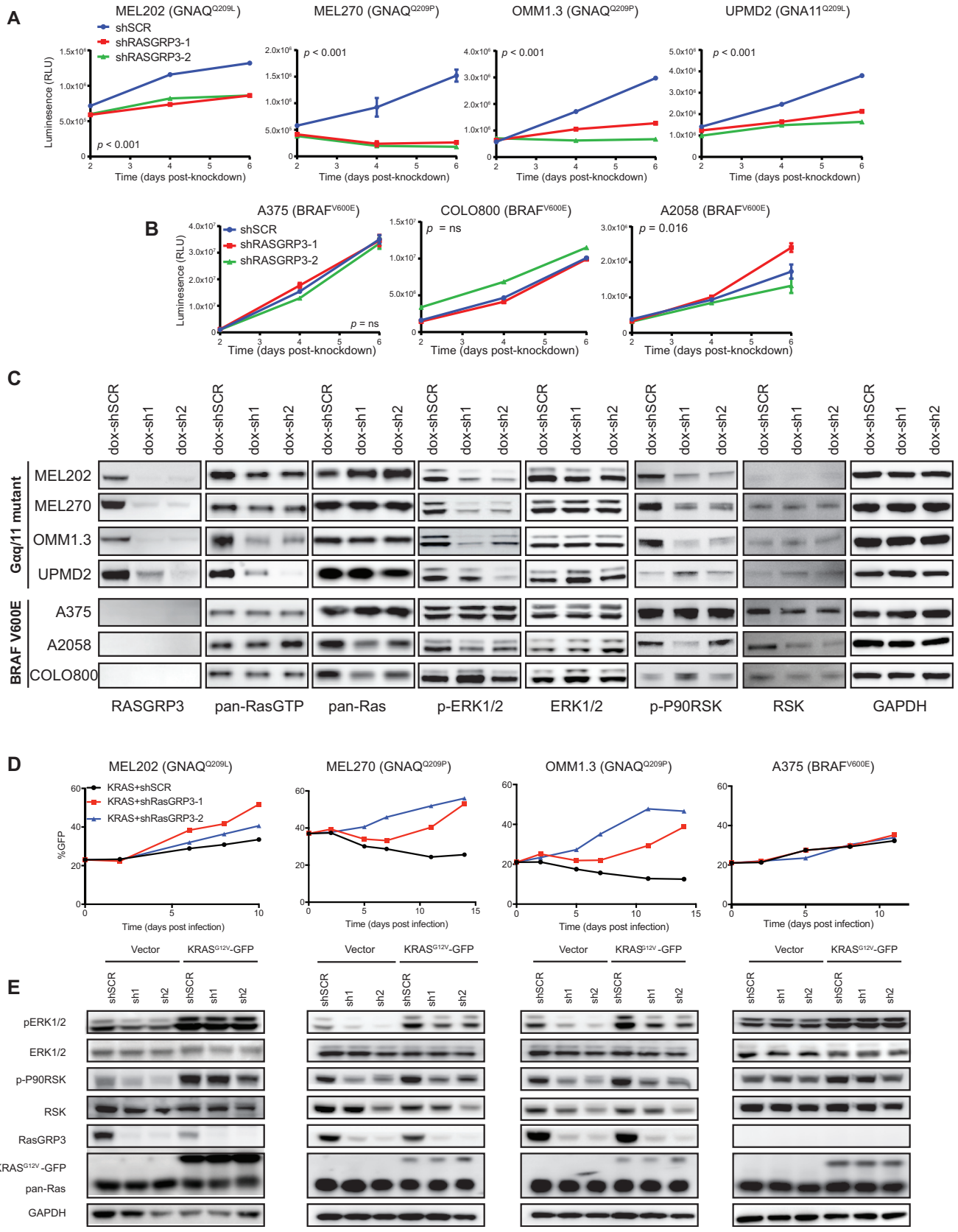

(legend on next page)

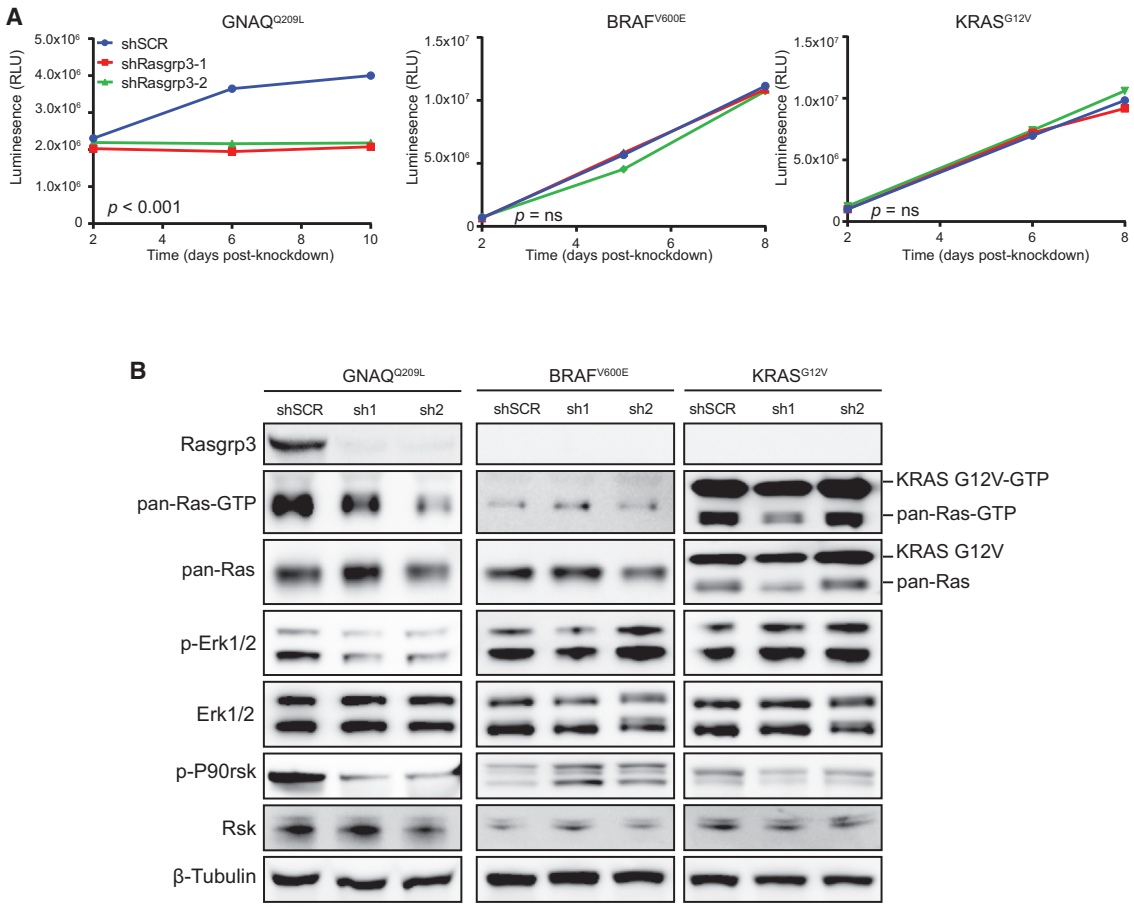

Figure 7. Rasgrp3 Is Required for Gα$_{11/q}$-Mediated Growth and MAPK Activation in Melan-a Cells

(A) Growth curves of GNAQ^{Q209L}, BRAF^{V600E}, or KRAS^{G12V} melan-a cells, grown in the absence of TPA and expressing shSCR, shRasgrp3-1, or shRasgrp3-2, shown as RLUs. Error bars, means ± SEM from six technical replicates. p < 0.001 (GNAQ^{Q209L}) and p = ns (BRAF^{V600E} and KRAS^{G12V}) for reduction in growth.

(B) Immunoblots of Rasgrp3 and MAPK pathway following Rasgrp3 depletion.

See also Figure S7.

exclusive cooperating mutations in *BAP1*, *SF3B1*, and *EIF1AX* that convey poor, intermediate, and favorable risk, respectively (de la Fouchardière et al., 2015; Goldman-Lévy et al., 2016; Küsters-Vandevelde et al., 2016). This distinct molecular profile is observed in a small subset of CMs and ~10% of mucosal melanomas (Sheng et al., 2016). Pathologically, UMs are characterized by their retention of the melanocyte lineage program, including pigmentation (Rothermel et al., 2016).

No proven effective therapies exist for UM. As with Ras, it is difficult to target G-proteins with competitive inhibitors to the nucleotide-binding site due to the high cellular concentrations of GTP. Since Gα$_{11/q}$ signaling activates PKC and the MAPK pathway, via PLCβ, many groups have studied the role of PKC and MAPK in UM. Cells with Gα$_{11/q}$ mutations were modestly sensitive to MEK inhibition and combination treatment of PKC and MEK inhibitors (Chen et al., 2014). Unfortunately, PKC targeting is limited by toxicity, and a completed phase 3 trial with selumetinib showed no clinical benefit (Komatsubara et al., 2016). In addition to PLCβ, Gα$_q$ directly interacts with the Trio family of Rho-GEFs (Trio, p63-RhoGEF, and Kalirin) to activate

Figure 6. RASGRP3 Is Required for Growth and ras Activation in UM Cells

(A and B) Growth curves of UM (A) or CM (B) cells with shSCR, shRASGRP3-1, or shRASGRP3-2, shown as relative luminescence units (RLUs). Error bars, means ± SEM from six technical replicates. p < 0.001 (A), p = not significant (ns), and p = 0.016 (B).

(C) Immunoblots of RASGRP3 and MAPK pathway. UM and CM cells stably expressing dox-shSCR, dox-shRASGRP3-1, or dox-shRASGRP3-2 in the presence of dox are shown.

(D) Percentage GFP-positive cells over time expressing KRAS^{G12V}-IRES-GFP with shSCR, shRASGRP3-1, or shRASGRP3-2. Change of percentage GFP-positive indicates relative growth of KRAS^{G12V}-expressing cells to non-expressing cells.

(E) Immunoblot of bulk cells (D) against the indicated proteins.

See also Figure S7.

Rac and Rho and downstream YAP, and this pathway may represent a therapeutic target (Feng et al., 2014; Yu et al., 2014). Another promising target is ARF6, a GTPase involved in vesicle trafficking and required for proper shuttling of activated $G\alpha_q$ to cytoplasmic vesicles, where downstream signaling to both PLCβ and Rho were localized (Yoo et al., 2016). In addition to $G\alpha_{11/q}$ signaling, another therapeutic strategy is targeting the melanocyte lineage. IMCgp100 is a bispecific antibody that binds gp100 (*PMEL*) on tumor cells and CD3 on T cells (Carvajal et al., 2014, J. Stem Cell Res. Ther., abstract). A phase 1 trial in melanoma showed a disease control rate of 21% and 57% in CM and UM, respectively, and an expanded study in UM showed a similar disease control rate with some durable responses (Iams et al., 2017).

Here we sought to generate a clinically relevant GEMM of aggressive $G\alpha_{11}$-driven melanoma, combining *GNA11*^{Q209L} and BAP1 loss, and we compared it to an isogenic *BRaf*^{V600E} model to identify $G\alpha_{11}$-driven phenotypes and vulnerabilities. We found GNA11^{Q209L} drove neoplastic growth in cutaneous and many non-cutaneous sites whereas BRaf^{V600E} only promotes CM. While the lung and lymph nodes are the preferential sites of metastasis in the *Tyr-CreER*^{T2}*;BRaf*$^{CA/+}$*;Pten*$^{flox/flox}$ mouse (Dankort et al., 2009) and in a transgenic mouse of *Tyr*-driven SV40 T-antigen (Bradl et al., 1991), one limitation in our mouse model was the inability to specifically activate *GNA11*^{Q209L} in defined melanocytic subsets, and this hampers the ability to definitively assign metastasis (Gibson et al., 2010; Klein-Szanto et al., 1991).

GNA11^{Q209L}-driven tumors were highly pigmented compared to BRaf^{V600E}, consistent with clinical observation that $G\alpha_{11/q}$-driven primary blue nevi, UM, and UM metastases retain pigmentation (Emley et al., 2011; Rothermel et al., 2016). Therefore, $G\alpha_{q/11}$ signaling drives lineage commitment, and targeting the lineage, such as IMCgp100, is a promising therapeutic strategy (Carvajal et al., 2014, J. Stem Cell Res. Ther., abstract). Bap1 loss in our GEMM accelerated skin melanoma growth, consistent with the clinical observation that BAP1 loss is found in transformed, but not benign, blue nevi (Griewank et al., 2017). Yet, there was no significant change of uveal pathology, highlighting a limitation of our model.

Cross-species comparison between representative GEMM models with human disease can identify critical mediators of tumorigenesis (Johnson et al., 2010). By cross-referencing the RNA-seq data from the GEMM and human disease data, we identified a Ras-GEF, RasGRP3, as a required signaling node for UM. Consistent with a recently published study (Chen et al., 2017), we observed RasGRP3 is highly upregulated in UM and is required for proliferation. We additionally showed engineered cells driven by mutant $G\alpha_{11/q}$ specifically require RasGRP3 for Ras activation and growth. *RASGPR3* expression is tissue specific and, among cancers, constrained to $G\alpha_{11/q}$-driven melanomas, leukemias, and lymphomas, suggesting RasGRP3 is a specific vulnerability in $G\alpha_{11/q}$-driven tumors and potentially a therapeutic target. The interaction between G-proteins and their GEFs is a viable drug target, as exemplified by the antibiotic brefeldin A, which blocks interaction between ARF1 and its GEF Sec7 (Mossessova et al., 2003), and RasGRP3 may be similarly targeted.

EXPERIMENTAL PROCEDURES

Further details and an outline of the resources used in this work can be found in the Supplemental Experimental Procedures.

Mouse Experiments

All animal studies were performed in accordance with the MSKCC IACUC (11-12-029). For GEMM studies, three cohorts of mice, *Tyr-CreER*^{T2}*;GNA11*^{Q209L}, *Tyr-CreER*^{T2}*;GNA11*^{Q209L}*;Bap1*$^{lox/lox}$, and *Tyr-CreER*^{T2}*;BRaf*$^{CA/+}$*;Bap1*$^{lox/lox}$, were administered with intraperitoneal tamoxifen at 4 weeks of age with no regard to the sex of the animals, and histology was similar between males and females. Mice developed tumors *in situ* after tamoxifen injection. Mice were euthanized in response but not limited to the following: tumors larger than 1 cm^3, tumor ulceration, tumors located too close to the trunk of the mice to impede movement and blood flow, and tumor burden, and time of euthanization was used for Kaplan-Meier survival analysis. For allograft studies, GEMM-derived tumors were grafted into 6- to 8-week-old female CB17-SCID mice and treated with vehicle or trametinib via oral gavage.

Histology, Immunohistochemistry, and Immunofluorescence

All tissues were fixed at 4°C overnight in 4% paraformaldehyde. Tissue processing, embedding, sectioning, H&E staining, and H&E staining with melanin bleaching were performed by Histoserv. Skull sections were performed following decalcification.

RNA-Seq

Total RNA was extracted from fresh-frozen tissue or cell lines using QIAGEN's RNeasy Mini Kit. The isolated RNA was processed for RNA-seq by the Integrated Genomics Core Facility at MSKCC.

Cell Lines

Melan-a cells were provided by D. Bennett (Bennett et al., 1987); MEL202, MEL270, OMM1.3, COLO800, UPMM3, A375, and A2058 cells were submitted for short tandem repeat (STR) profiling and MSK-IMPACT (integration mutation profiling of actionable cancer targets) for mutational status at MSKCC to confirm their authenticity.

Statistics

Boxplots represent 25th and 75th percentiles with midline indicating the median; whiskers extend to the lowest/highest value within 1.5 times the interquartile range. Outliers are shown as dots. Comparisons for growth curves and xenograft experiments between two groups were performed using a two-tailed parametric unpaired t test. All statistics were performed using GraphPad Prism 6.0 software.

DATA AND SOFTWARE AVAILABILITY

The accession number for the data reported in this paper is GEO: GSE97225.

SUPPLEMENTAL INFORMATION

Supplemental Information includes Supplemental Experimental Procedures, seven figures, and three tables and can be found with this article online at https://doi.org/10.1016/j.celrep.2018.01.081.

ACKNOWLEDGMENTS

We gratefully acknowledge David Abramson, Brian Marr, Irina Belinsky, and Taha Merghoub for their intellectual input. Next-generation sequencing and gene expression arrays were done at the MSKCC Integrated Genomics Operation. Gene targeting was performed by the Rockefeller University Gene Targeting Facility (Chingweng Yang), and blastocyst injection was performed by the MSKCC Mouse Genetic Facility (Willie Marks). FACS was performed at the MSKCC Flow Cytometry Core. Mouse pathology was reviewed by the MSKCC Laboratory of Comparative Pathology Core Facility. This work was supported by MSKCC Support Grant/Core Grant (P30 CA008748) and grants

from the NCI (K08CA140946, Y.C.; R01CA193837, Y.C.; P50CA092629, Y.C.; P50CA140146, P.C.; K08CA151660, P.C.; and DP2 CA174499, P.C.), US DOD (W81XWH-10-1-0197, P.C.), the Prostate Cancer Foundation (16CHAL03, Y.C.), the Starr Cancer Consortium (I7-A722, Y.C. and P.C.), the Geoffrey Beene Cancer Research Center (Y.C. and P.C.), the Gerstner Family Foundation (Y.C.), Bressler Scholars Fund (Y.C.), and Cycle for Survival (Y.C.).

AUTHOR CONTRIBUTIONS

Project Planning and Experimental Design, P.C., Y.C., A.R.M., L.R., K.G.G., and A.N.S.; Pathology Review, R.M. and S.M.; Bioinformatics, Y.C. and A.R.M.; Cellular Assays, A.R.M., L.R., Y.G., and T.D.H.; Mice, A.R.M., J.J.S., and E.G.W.; Expression Vectors, A.R.M., Y.G., J.Q.Z., C.H., and T.W.; Manuscript Writing, A.R.M., P.C., and Y.C.; Review of the Final Manuscript, all authors.

DECLARATION OF INTERESTS

The authors declare no competing interests.

Received: May 1, 2017
Revised: October 30, 2017
Accepted: January 26, 2018
Published: February 27, 2018

REFERENCES

Aiba, Y., Oh-hora, M., Kiyonaka, S., Kimura, Y., Hijikata, A., Mori, Y., and Kurosaki, T. (2004). Activation of RasGRP3 by phosphorylation of Thr-133 is required for B cell receptor-mediated Ras activation. Proc. Natl. Acad. Sci. USA *101*, 16612–16617.

Alizadeh, A., Fitch, K.R., Niswender, C.M., McKnight, G.S., and Barsh, G.S. (2008). Melanocyte-lineage expression of Cre recombinase using Mitf regulatory elements. Pigment Cell Melanoma Res. *21*, 63–69.

Ambrosini, G., Pratilas, C.A., Qin, L.X., Tadi, M., Surriga, O., Carvajal, R.D., and Schwartz, G.K. (2012). Identification of unique MEK-dependent genes in GNAQ mutant uveal melanoma involved in cell growth, tumor cell invasion, and MEK resistance. Clin. Cancer Res. *18*, 3552–3561.

Aoki, H., Yamada, Y., Hara, A., and Kunisada, T. (2009). Two distinct types of mouse melanocyte: differential signaling requirement for the maintenance of non-cutaneous and dermal versus epidermal melanocytes. Development *136*, 2511–2521.

Bennett, D.C., Cooper, P.J., and Hart, I.R. (1987). A line of non-tumorigenic mouse melanocytes, syngeneic with the B16 melanoma and requiring a tumour promoter for growth. Int. J. Cancer *39*, 414–418.

Bradl, M., Klein-Szanto, A., Porter, S., and Mintz, B. (1991). Malignant melanoma in transgenic mice. Proc. Natl. Acad. Sci. USA *88*, 164–168.

Cancer Genome Atlas, N.; Cancer Genome Atlas Network (2015). Genomic Classification of Cutaneous Melanoma. Cell *161*, 1681–1696.

Carvajal, R.D., Sosman, J.A., Quevedo, J.F., Milhem, M.M., Joshua, A.M., Kudchadkar, R.R., Linette, G.P., Gajewski, T.F., Lutzky, J., Lawson, D.H., et al. (2014). Effect of selumetinib vs chemotherapy on progression-free survival in uveal melanoma: a randomized clinical trial. JAMA *311*, 2397–2405.

Chen, X., Wu, Q., Tan, L., Porter, D., Jager, M.J., Emery, C., and Bastian, B.C. (2014). Combined PKC and MEK inhibition in uveal melanoma with GNAQ and GNA11 mutations. Oncogene *33*, 4724–4734.

Chen, X., Wu, Q., Depeille, P., Chen, P., Thornton, S., Kalirai, H., Coupland, S.E., Roose, J.P., and Bastian, B.C. (2017). RasGRP3 Mediates MAPK Pathway Activation in GNAQ Mutant Uveal Melanoma. Cancer Cell *31*, 685–696.e6.

Collaborative Ocular Melanoma Study Group (2001). Assessment of metastatic disease status at death in 435 patients with large choroidal melanoma in the Collaborative Ocular Melanoma Study (COMS): COMS report no. 15. Arch. Ophthalmol. *119*, 670–676.

Dankort, D., Curley, D.P., Cartlidge, R.A., Nelson, B., Karnezis, A.N., Damsky, W.E., Jr., You, M.J., DePinho, R.A., McMahon, M., and Bosenberg, M. (2009). Braf(V600E) cooperates with Pten loss to induce metastatic melanoma. Nat. Genet. *41*, 544–552.

de la Fouchardière, A., Cabaret, O., Pètre, J., Aydin, S., Leroy, A., de Potter, P., Pissaloux, D., Haddad, V., Bressac-de Paillerets, B., and Janin, N. (2015). Primary leptomeningeal melanoma is part of the BAP1-related cancer syndrome. Acta Neuropathol. *129*, 921–923.

Diener-West, M., Reynolds, S.M., Agugliaro, D.J., Caldwell, R., Cumming, K., Earle, J.D., Hawkins, B.S., Hayman, J.A., Jaiyesimi, I., Jampol, L.M., et al.; Collaborative Ocular Melanoma Study Group (2005). Development of metastatic disease after enrollment in the COMS trials for treatment of choroidal melanoma: Collaborative Ocular Melanoma Study Group Report No. 26. Arch. Ophthalmol. *123*, 1639–1643.

Emley, A., Nguyen, L.P., Yang, S., and Mahalingam, M. (2011). Somatic mutations in GNAQ in amelanotic/hypomelanotic blue nevi. Hum. Pathol. *42*, 136–140.

Feng, X., Degese, M.S., Iglesias-Bartolome, R., Vaque, J.P., Molinolo, A.A., Rodrigues, M., Zaidi, M.R., Ksander, B.R., Merlino, G., Sodhi, A., et al. (2014). Hippo-independent activation of YAP by the GNAQ uveal melanoma oncogene through a trio-regulated rho GTPase signaling circuitry. Cancer Cell *25*, 831–845.

Furney, S.J., Pedersen, M., Gentien, D., Dumont, A.G., Rapinat, A., Desjardins, L., Turajlic, S., Piperno-Neumann, S., de la Grange, P., Roman-Roman, S., et al. (2013). SF3B1 mutations are associated with alternative splicing in uveal melanoma. Cancer Discov. *3*, 1122–1129.

Gibson, P., Tong, Y., Robinson, G., Thompson, M.C., Currle, D.S., Eden, C., Kranenburg, T.A., Hogg, T., Poppleton, H., Martin, J., et al. (2010). Subtypes of medulloblastoma have distinct developmental origins. Nature *468*, 1095–1099.

Goldman-Lévy, G., Rigau, V., Bléchet, C., Bens, G., Muckensturm, B., Delage, M., Labrousse, F., Haddad, V., Attignon, V., Pissaloux, D., and de la Fouchardière, A. (2016). Primary Melanoma of the Leptomeninges with BAP1 Expression-Loss in the Setting of a Nevus of Ota: A Clinical, Morphological and Genetic Study of 2 Cases. Brain Pathol. *26*, 547–550.

Griewank, K.G., Yu, X., Khalili, J., Sozen, M.M., Stempke-Hale, K., Bernatchez, C., Wardell, S., Bastian, B.C., and Woodman, S.E. (2012). Genetic and molecular characterization of uveal melanoma cell lines. Pigment Cell Melanoma Res. *25*, 182–187.

Griewank, K.G., Müller, H., Jackett, L.A., Emberger, M., Möller, I., van de Nes, J.A., Zimmer, L., Livingstone, E., Wiesner, T., Scholz, S.L., et al. (2017). SF3B1 and BAP1 mutations in blue nevus-like melanoma. Mod. Pathol. *30*, 928–939.

Harbour, J.W., Onken, M.D., Roberson, E.D., Duan, S., Cao, L., Worley, L.A., Council, M.L., Matatall, K.A., Helms, C., and Bowcock, A.M. (2010). Frequent mutation of BAP1 in metastasizing uveal melanomas. Science *330*, 1410–1413.

Huang, J.L., Urtatiz, O., and Van Raamsdonk, C.D. (2015). Oncogenic G Protein GNAQ Induces Uveal Melanoma and Intravasation in Mice. Cancer Res. *75*, 3384–3397.

Iams, W.T., Sosman, J.A., and Chandra, S. (2017). Novel Targeted Therapies for Metastatic Melanoma. Cancer J. *23*, 54–58.

Infante, J.R., Fecher, L.A., Falchook, G.S., Nallapareddy, S., Gordon, M.S., Becerra, C., DeMarini, D.J., Cox, D.S., Xu, Y., Morris, S.R., et al. (2012). Safety, pharmacokinetic, pharmacodynamic, and efficacy data for the oral MEK inhibitor trametinib: a phase 1 dose-escalation trial. Lancet Oncol. *13*, 773–781.

Johansson, P., Aoude, L.G., Wadt, K., Glasson, W.J., Warrier, S.K., Hewitt, A.W., Kiilgaard, J.F., Heegaard, S., Isaacs, T., Franchina, M., et al. (2016). Deep sequencing of uveal melanoma identifies a recurrent mutation in PLCB4. Oncotarget *7*, 4624–4631.

Johnson, R.A., Wright, K.D., Poppleton, H., Mohankumar, K.M., Finkelstein, D., Pounds, S.B., Rand, V., Leary, S.E., White, E., Eden, C., et al. (2010). Cross-species genomics matches driver mutations and cell compartments to model ependymoma. Nature *466*, 632–636.

Klein-Szanto, A., Bradl, M., Porter, S., and Mintz, B. (1991). Melanosis and associated tumors in transgenic mice. Proc. Natl. Acad. Sci. USA *88*, 169–173.

Komatsubara, K.M., Manson, D.K., and Carvajal, R.D. (2016). Selumetinib for the treatment of metastatic uveal melanoma: past and future perspectives. Future Oncol. *12*, 1331–1344.

Küsters-Vandevelde, H.V., Creytens, D., van Engen-van Grunsven, A.C., Jeunink, M., Winnepenninckx, V., Groenen, P.J., Küsters, B., Wesseling, P., Blokx, W.A., and Prinsen, C.F. (2016). SF3B1 and EIF1AX mutations occur in primary leptomeningeal melanocytic neoplasms; yet another similarity to uveal melanomas. Acta Neuropathol. Commun. *4*, 5.

LaFave, L.M., Béguelin, W., Koche, R., Teater, M., Spitzer, B., Chramiec, A., Papalexi, E., Keller, M.D., Hricik, T., Konstantinoff, K., et al. (2015). Loss of BAP1 function leads to EZH2-dependent transformation. Nat. Med. *21*, 1344–1349.

Lito, P., Saborowski, A., Yue, J., Solomon, M., Joseph, E., Gadal, S., Saborowski, M., Kastenhuber, E., Fellmann, C., Ohara, K., et al. (2014). Disruption of CRAF-mediated MEK activation is required for effective MEK inhibition in KRAS mutant tumors. Cancer Cell *25*, 697–710.

Martin, M., Maßhöfer, L., Temming, P., Rahmann, S., Metz, C., Bornfeld, N., van de Nes, J., Klein-Hitpass, L., Hinnebusch, A.G., Horsthemke, B., et al. (2013). Exome sequencing identifies recurrent somatic mutations in EIF1AX and SF3B1 in uveal melanoma with disomy 3. Nat. Genet. *45*, 933–936.

Möller, I., Murali, R., Müller, H., Wiesner, T., Jackett, L.A., Scholz, S.L., Cosgarea, I., van de Nes, J.A., Sucker, A., Hillen, U., et al. (2017). Activating cysteinyl leukotriene receptor 2 (CYSLTR2) mutations in blue nevi. Mod. Pathol. *30*, 350–356.

Moore, A.R., Ceraudo, E., Sher, J.J., Guan, Y., Shoushtari, A.N., Chang, M.T., Zhang, J.Q., Walczak, E.G., Kazmi, M.A., Taylor, B.S., et al. (2016). Recurrent activating mutations of G-protein-coupled receptor CYSLTR2 in uveal melanoma. Nat. Genet. *48*, 675–680.

Mossessova, E., Corpina, R.A., and Goldberg, J. (2003). Crystal structure of ARF1*Sec7 complexed with Brefeldin A and its implications for the guanine nucleotide exchange mechanism. Mol. Cell *12*, 1403–1411.

Rebhun, J.F., Castro, A.F., and Quilliam, L.A. (2000). Identification of guanine nucleotide exchange factors (GEFs) for the Rap1 GTPase. Regulation of MR-GEF by M-Ras-GTP interaction. J. Biol. Chem. *275*, 34901–34908.

Robertson, A.G., Shih, J., Yau, C., Gibb, E.A., Oba, J., Mungall, K.L., Hess, J.M., Uzunangelov, V., Walter, V., Danilova, L., et al.; TCGA Research Network (2017). Integrative Analysis Identifies Four Molecular and Clinical Subsets in Uveal Melanoma. Cancer Cell *32*, 204–220.e15.

Rothermel, L.D., Sabesan, A.C., Stephens, D.J., Chandran, S.S., Paria, B.C., Srivastava, A.K., Somerville, R., Wunderlich, J.R., Lee, C.C., Xi, L., et al. (2016). Identification of an Immunogenic Subset of Metastatic Uveal Melanoma. Clin. Cancer Res. *22*, 2237–2249.

Sheng, X., Kong, Y., Li, Y., Zhang, Q., Si, L., Cui, C., Chi, Z., Tang, B., Mao, L., Lian, B., et al. (2016). GNAQ and GNA11 mutations occur in 9.5% of mucosal melanoma and are associated with poor prognosis. Eur. J. Cancer *65*, 156–163.

Solit, D.B., Garraway, L.A., Pratilas, C.A., Sawai, A., Getz, G., Basso, A., Ye, Q., Lobo, J.M., She, Y., Osman, I., et al. (2006). BRAF mutation predicts sensitivity to MEK inhibition. Nature *439*, 358–362.

Tandon, N., O'Neill, T.J., Vollmer, D.G., and Wang, M. (2008). Intraventricular occurrence of a melanocytoma. J. Neurosurg. *109*, 480–485.

Van Raamsdonk, C.D., Bezrookove, V., Green, G., Bauer, J., Gaugler, L., O'Brien, J.M., Simpson, E.M., Barsh, G.S., and Bastian, B.C. (2009). Frequent somatic mutations of GNAQ in uveal melanoma and blue naevi. Nature *457*, 599–602.

Van Raamsdonk, C.D., Griewank, K.G., Crosby, M.B., Garrido, M.C., Vemula, S., Wiesner, T., Obenauf, A.C., Wackernagel, W., Green, G., Bouvier, N., et al. (2010). Mutations in GNA11 in uveal melanoma. N. Engl. J. Med. *363*, 2191–2199.

Wellbrock, C., Ogilvie, L., Hedley, D., Karasarides, M., Martin, J., Niculescu-Duvaz, D., Springer, C.J., and Marais, R. (2004). V599EB-RAF is an oncogene in melanocytes. Cancer Res. *64*, 2338–2342.

Yoo, J.H., Shi, D.S., Grossmann, A.H., Sorensen, L.K., Tong, Z., Mleynek, T.M., Rogers, A., Zhu, W., Richards, J.R., Winter, J.M., et al. (2016). ARF6 Is an Actionable Node that Orchestrates Oncogenic GNAQ Signaling in Uveal Melanoma. Cancer Cell *29*, 889–904.

Yu, F.X., Luo, J., Mo, J.S., Liu, G., Kim, Y.C., Meng, Z., Zhao, L., Peyman, G., Ouyang, H., Jiang, W., et al. (2014). Mutant Gq/11 promote uveal melanoma tumorigenesis by activating YAP. Cancer Cell *25*, 822–830.

Zheng, Y., Liu, H., Coughlin, J., Zheng, J., Li, L., and Stone, J.C. (2005). Phosphorylation of RasGRP3 on threonine 133 provides a mechanistic link between PKC and Ras signaling systems in B cells. Blood *105*, 3648–3654.

Cell Reports, Volume *22*

Supplemental Information

GNA11 Q209L Mouse Model Reveals RasGRP3 as an Essential Signaling Node in Uveal Melanoma

Amanda R. Moore, Leili Ran, Youxin Guan, Jessica J. Sher, Tyler D. Hitchman, Jenny Q. Zhang, Catalina Hwang, Edward G. Walzak, Alexander N. Shoushtari, Sébastien Monette, Rajmohan Murali, Thomas Wiesner, Klaus G. Griewank, Ping Chi, and Yu Chen

SUPPLEMENTAL EXPERIMENTAL PROCEDURES

Genetically Engineered Mice

We cloned in human *GNA11*^{Q209L} with an internal glu-glu tag (Van Raamsdonk et al., 2010) into a modified pBTG (Murtaugh et al., 2003) (Addgene plasmid 268) with LoxP sites reversed to remove the forward ATG codon within LoxP site and into Rosa26 locus as previously described (Addgene 15036) (Chen et al., 2013).

Gene targeting was performed at the Rockefeller University Gene Targeting Resource Center (Head: Chingwen Yang). The targeting plasmid was electrophoresed into albino C57BL/6J ES cells and G418 resistant clones were isolated by standard procedures. The clones were screened by Southern blotting. Two positive clones were injected into C57BL/6J blastocysts by the MSKCC Mouse Genetics Core Facility (Head: Willie Mark) and chimeras were mated with albino C57BL/6J females. Germline transmission was confirmed in albino offspring using Southern blotting. For subsequent generations, *GNA11*^{Q209L} mouse genotyping was performed by qPCR of genomic DNA using primers listed in **Table S2**.

Bap1$^{flox/flox}$ (C57BL/6N-Bap1tm1c(EUCOMM)Hmgu/Wtsi) mice were purchased from EUCOMM (LaFave et al., 2015). Tyrosinase-CreERT2 and BRaf^{V600E} mice were obtained from Jackson Labs [B6.Cg-Tg(Tyr-cre/ERT2)13Bos/J (012328); B6.129P2(Cg)-Braftm1Mmcm/J (017837)](Bosenberg et al., 2006). CAG-LSL-EYFP (also known as Ai3) mice (Madisen et al., 2010) were obtained from Jackson Labs [B6.Cg-Gt(ROSA)26Sortm3(CAG-EYFP)Hze/J (007903)]. Standard PCR was performed for genotyping of Tyr-CreERT2, BRaf^{CA}, Bap1$^{flox/flox}$ are listed in Table S2.

Mouse survival was determined under the recommendation of MSKCC veterinary services or upon encountering mice undergoing visible discomfort and in accordance to the MSKCC Institutional Animal Care and Use Committee (IACUC 11-12-029). In accordance to our animal protocol, mice were euthanized in response but not limited to the following: tumors larger than 1cm^3, tumor ulceration, tumors located too close to the trunk of the mice to impeded movement and blood flow and tumor burden.

Intraperitoneal injection of tamoxifen was performed at 4-weeks of age with no regard to the sex of the animals and histology was similar between both males and females.

Allograft and Treatment

Tumors from *Tyr-CreER*^{T2};*Braf*^{V600E};*Bap1*^{KO} and *Tyr-CreER*^{T2};*GNA11*^{Q209L};*Bap1*^{KO} mice were expanded in 6-8 week old C.B17-scid mice (C.B-*Igh-1*^{b}/IcrTac-*Prkdc*^{scid}; Taconic) and then serial grafted bilaterally using equal size tumors. The experimental cohort of mice 6-8 week old female C.B17-scid mice (Taconic) of 8 tumors for the vehicle and trametinib treated *Tyr-CreER*^{T2};*GNA11*^{Q209L};*Bap1*^{KO} and 24 tumors for the trametinib treated arm and 7 tumors for the control arm for *Tyr-CreER*^{T2};*Braf*^{V600E};*Bap1*^{KO} tumors. The size of each cohort was determined on the basis of previous experiments without specific statistical methods. Mice we treated with 3mg kg^{-1} trametinib (Active Biochem) dissolved in trametinib solvent (30% PEG-400, 0.5% TWEEN® 80, 5% propylene glycol in PBS) once daily for 5 days a week. Tumors were measured with calipers every 2 or 3 days for up to 25 days with trametinib treatment and were actively measured for at least 10 days before treatment. Tumor growth curves were visualized with Prism GraphPad 6.0. Tumor volume was calculated using the formula: $\text{volume} = \frac{\pi(length)(width)(height)}{6}$.

Histology and immunohistochemistry

Prior to immunohistochemistry, melanin bleaching was performed using a delicate melanin bleach kit (Polysciences Inc.) according to the manufacturer's instructions. Immunohistochemistry for HMB45, DT101, BC199 melanoma cocktail (Abcam, ab732, 1:50), MITF (Cell Signaling Technology, 12590, 1:50), Ki-67 (Abcam, ab16667, 1:100) antibodies were diluted in SignalStain antibody diluent (Cell Signaling Technology). Staining was performed using a standard multimer/diaminobenzidine (DAB) detection protocol for MITF and Ki67 and red chromogen staining (alkaline phosphatase; Ventana; UltraMap Red) for the melanoma cocktail following epitope retrieval with citrate (Ventana; CC1), hematoxylin counterstain on a Discovery Ultra system (Roche/Ventana) with appropriate negative and positive controls. Immunohistochemistry for each tissue shown was preformed on tissues harvested from at least 5 animals.

Immunofluorescence of eye and skin

All tissues were fixed at room temperature for 30min in 4% paraformaldehyde (Electron Microscopy Sciences). Tissues were then incubated in 30% sucrose in PBS at 4°C overnight, washed once with PBS, embed in OCT, flash frozen and cut into 5 µM sections using a cryostat. Tissue sections were blocked for 1 hour using 5% goat serum, incubated with Gp100 antibody at 4 °C overnight and secondary antibody for 2 hours at room temperature. Slides were mounted using PBS with 1ug ml^{-1} DAPI for direct visualization of YFP and Gp100. Images were taken on a Nikon Eclipse TE2000-E microscope using a Photometric Coolsnap HQ camera. Images were taken with ×20 (numerical aperture 0.75) objectives. Monochrome images taken with DAPI, YFP and Texas Red filter sets were pseudo-colored blue, green and red, respectively, and merged using ImageJ.

Intraperitoneal injection of tamoxifen was administered in both sexes of the animals and histology was similar between both males and females. At least 45 animals for each genotype ($GNA11^{Q209L}$, $GNA11^{Q209L}$; $Bap1^{lox/lox}$, $Bap1^{lox/lox}$, $BRaf^{V600E}$; $Bap1^{lox/lox}$) were injected with tamoxifen and observed. At least 14 animals for each genotype underwent a full necropsy and were tissues evaluated by H&E.

RNA-seq

For mouse tumors, total RNA was extracted from fresh-frozen tissue or cell lines using Qiagen's RNeasy Mini Kit (Qiagen). The isolated RNA was processed for RNA-sequencing by the Integrated Genomics Core Facility at MSKCC. The libraries were sequenced on an Illumina HiSeq-2500 platform with 51 bp paired-end reads to obtain a minimum yield of 40 million reads per sample. The sequence data were mapped to the mouse reference genome (mm9) and the number of reads was quantified using STAR v2.330 (Dobin et al., 2013).

For UPMM3 cells, the libraries were sequenced on an Illumina HiSeq-2500 platform with 51 bp single-end reads to obtain a minimum yield of 40 million reads per sample. The sequence data were mapped to the human reference genome (hg19) and the number of reads was quantified using Cufflinks (Roberts et al., 2011). GSEA was performed using JAVA GSEA 2.0 program (Subramanian et al., 2005). The gene sets used for analysis were the Broad Molecular Signatures Database gene sets c2 (curated gene sets), c5 (gene ontology gene sets), c6 (oncogenic signatures). GSEA enrichment sets are shown in **Table S1**.

Level 3 RNA-seqV2 data for TCGA uveal melanoma (n=80) and cutaneous melanoma (SKCM; n=471) were downloaded from NIH TCGA server. We merged the samples and annotated them by mutational status ($BRAF^{V600E}$, GNAQ or GNA11 at R183 or Q209) and by tissue source (primary or metastatic). Differential gene expression was performed using ANOVA analysis with the Partek Genomics Suite 6.6 in both the TCGA and genetically engineered mouse model datasets. Expression of RASGRP3 from pan-TCGA cancers was downloaded from cBioportal (Cerami et al., 2012) and from Gene Expression across Normal and Tumor tissue (GENT) (Shin et al., 2011) was downloaded from http://medicalgenome.kribb.re.kr/GENT/.

Ki-67 quantification

Following immunohistochemistry for Ki-67, 10 randomly selected field images at 40 x magnifications were taken. These images were converted to greyscale, threshold adjusted, and particles were analyzed using ImageJ v1.60 (NIH) automated counting to determine the number of cells per field. The same parameters were used throughout quantification. To determine the percent of cells that were positive for Ki-67, we performed identical procedures while optimizing the threshold to include only cells with positive DAB staining. The same parameters were used throughout quantification.

PCR for Bap1 lox/lox excision

DNA from Bap1 mice was isolated using DNeasy Blood & Tissue Kit (Qiagen). DNA from whole cutaneous tumors and dissected uveal tracts were used for the PCR. Control tissues were isolated from mouse toes. PCR of genomic DNA was performed using primers listed in **Table S2**.

Cell lines

Melan-a cells were provided by D. Bennett (St. George's Hospital, University of London, London, UK)(Bennett et al., 1987) and were grown in RPMI with 200nM 12-O-Tetradecanoylphorbol-13-Acetate (TPA; Sigma-Aldrich) before stable expression. Melan-a cells stably expressing $GNAQ^{Q209L}$, $BRAF^{V600E}$ and $KRAS^{G12V}$ were propagated in the absence of TPA. MEL202, MEL270, OMM1.3, COLO800 cells were grown in RPMI. UPMD1, UPMD2 and UPMM3 cells were grown in Ham's F12 media. A375 and A2058 cells were grown in DMEM media. 293T cells were used for retrovirus and lentivirus production and maintained in DMEM media. All cell culture media contained 10% FBS, penicillin (100 U ml^{-1}), streptomycin (100 µg ml^{-1}), L-glutamine (2mM). All cells were grown in a humidified incubator at 37 °C with 5% CO_2 and were tested regularly for mycoplasma contamination. All cell lines used were negative for mycoplasma. All uveal melanoma cell lines were validated for mutations status by MSK-IMPACT.

Proliferation and survival assays

Growth curves were performed following shRNA infection and around 1,000–3,000 cells were plated in a 96-well plate 24 hours following infection. Every 48 hours following infection, the number of cells was determined using a CelltiterGlo assay (Promega). IC_{50} assays were performed by plating 1,000–3,000 cells in a 96-well plate, allowed to adhere overnight, and then incubated with either fresh media containing trametinib. After 5 days, the number of cells was determined using a CelltiterGlo assay. Representative experiments are shown. Cell growth was assessed in three independent experiments, each in quadruplet.

Immunoblotting

Whole cell lysates were prepared in cell lysis buffer (Cell Signaling Technology) containing freshly added protease and phosphatase inhibitors (PhosSTOP, Roche, cOmplete EDTA-Free, Roche). Tumor lysates were generated by homogenization of flash-frozen tissue in cell lysis buffer (Cell Signaling Technology) containing freshly added protease and phosphatase inhibitors (PhosSTOP, Roche, cOmplete EDTA-Free, Roche). Equal amounts of protein, as measured by BCA protein assay (Thermo Scientific), were resolved on NuPAGE Novex 4-12% Bis-Tris Protein Gels (Life Technologies) and transferred electrophoretically onto a 0.45µm nitrocellulose membrane (Bio-Rad). Membranes were blocked for 1 hour at room temperature in StartingBlock TBS (Thermo Scientific) or Odyssey blocking buffer (LI-COR) before being incubated overnight at 4°C with the primary antibodies diluted at 1:1000 unless otherwise noted in either StartingBlock or Odyssey blocking buffer. The following primary antibodies were used (Cell Signaling unless noted otherwise): phospho-p44/42 MAPK (Erk1/2) (Thr202/Tyr204; 4370), p44/42 MAPK (Erk1/2;4695), phospho-$P90^{RSK}$ (Ser380;12032), RSK1/2/3 (9355), RasGRP3 (3334), Ras (8832), CyclinD1 (2922), SPRY4 (Santa Cruz Biotechnology; sc-30051), BAP1 (Santa Cruz Biotechnology; sc-28383), HA-tag (Roche; 3F10), GNAQ (abcam; ab199533), GAPDH (1:5,000

dilution; Applied Biological Materials, G041), β-actin (1:5,000 dilution; abcam, AC15). The Ras-GTP assay was performed according to manufactures instructions (Cell Signaling; 8821).

shRNA and inhibitors

For shRNA mediated knockdown of RASGRP3 the following hairpins were used with sequences listed in **Table S3**. Human shRASGRP3-1 and shRASGRP3-2 were obtained from the MSKCC RNAi Core in pLKO.1 and were subcloned into Tet-pLKO-puro (Wiederschain et al., 2009) (Addgene plasmid 21915). Mouse shRasgrp3-1 and shRasgrp3-2 were obtained from the MSKCC RNAi Core in pLKO.1. Stable expressing Tet-ON shRasGRP3 were induced with doxycycline 1μg ml^{-1} (Research Products International) and cells were harvested for protein 72 hours post-doxycycline addition. Melan-a cells were treated with the indicated dose of trametinib (SelleckChem). Cell growth for the half-maximal inhibitory concentration (IC_{50}) was assessed using CellTiter-Glo (Promega) five days post trametinib treatment.

Exogenous gene expression

Melan-a cells were stably transduced with: BRAF V600E, MSCV-HA-FLAG-BRAF-V600E. MSCV-HA-FLAG-V600E was cloned using the gateway method using pDONOR-BRAF (Addgene plasmid 70300) and subcloned into MSCV-HA-FLAG-puro-Dest. Site directed mutagenesis was performed using QuikChange (Agilent) to wild-type *BRAF* to introduce a p.Val600Glu mutation to give $BRAF^{V600E}$. KRAS G12V: MSCV-GFP-KRAS G12V, KRAS G12V (Addgene plasmid 31200) (Yang et al., 2011) was subcloned into MSCV-IRES-GFP-Dest using the gateway method. GNAQ Q209L: MSCV-puro-GNAQ Q209L, cDNA for the wild-type human *GNAQ* was obtained from Origene (sc128110) and cloned into MSCV-puro (Addgene plasmid 24828)(Olive et al., 2009). Site directed mutagenesis was performed using QuikChange (Agilent) to wild-type *GNAQ* to introduce a p.Gln209Leu mutation to give $GNAQ^{Q209L}$. QuikChange primers are listed in **Table S2**. The sequences of all constructs were confirmed by Sanger sequencing.

Resource Table

REAGENT or RESOURCE	SOURCE	IDENTIFIER
Antibodies		
Rabbit monoclonal anti-phospho-p44/42 MAPK (Erk1/2) (Thr202/Tyr204)	Cell Signaling Technology	Cat#4370; RRID: AB_2315112
Rabbit monoclonal anti-p44/42 MAPK (Erk1/2)	Cell Signaling Technology	Cat#4695; RRID: AB_390779
Rabbit monoclonal anti-Phospho-p90RSK (Ser380)	Cell Signaling Technology	Cat#;12032
Rabbit monoclonal anti-RSK1/RSK2/RSK3	Cell Signaling Technology	Cat#9355; RRID: AB_659900
Rabbit monoclonal anti-RASGRP3	Cell Signaling Technology	Cat#3334; RRID: AB_2269292
Mouse monoclonal anti-RAS	Cell Signaling Technology	Cat#8832
Rat monoclonal anti-HA (hemagglutinin)	Roche	Cat#3F10; RRID: AB_2314622
Rabbit monoclonal anti-GNAQ	Abcam	Cat#ab199533
Mouse monoclonal anti-BAP1 (C-4)	Santa Cruz Biotechnology	Cat# sc-28383; RRID:AB_626723
Rabbit monoclonal anti-Ki67 [SP6]	Abcam	Cat# ab16667, RRID:AB_302459
Rabbit monoclonal anti-MITF	Cell Signaling Technology	Cat# 12590, RRID:AB_2616024
Rabbit polyclonal anti-SPRY4	Santa Cruz Biotechnology	Cat# sc-30051 RRID:AB_2195449
Rabbit monoclonal anti-CyclinD1	Cell Signaling Technology	Cat# 2922 RRID:AB_2228523

Rabbit monoclonal anti-Melanoma gp100	Abcam	Cat#ab137078
Mouse monoclonal anti-Melanoma antibody [HMB45 + DT101 + BC199]	Abcam	Cat# ab732, RRID:AB_305844
Biological Samples		
Genetically engineered mouse tissues	This paper	N/A
Chemicals, Peptides, and Recombinant Proteins		
Trametinib (GSK1120212; mouse treatment)	Active Biochem	Cat#: A-1258; CAS: 871700-17-3
Trametinib (GSK1120212; cell treatment)	Selleck Chemicals	S2673; CAS: 871700-17-3
Critical Commercial Assays		
Ras-GTP	Cell Signaling Technology	Cat#8821
CellTiterGlo	Promega	G9242
Deposited Data		
Raw and analyzed RNA-sequencing data	This paper	GEO: GSE97225
Mendeley raw data	This paper	doi:10.17632/g2v849vzzm doi:10.17632/my5g8mdrkg doi:10.17632/8r58nb2ttc
Experimental Models: Cell Lines		
Mouse: Melan-a	(Bennett et al., 1987)	Wellcome Trust Functional Genomics Cell Bank; RRID:CVCL_4624
Human: MEL202	(Griewank et al., 2012)	RRID:CVCL_C301
Human: MEL270	(Griewank et al., 2012)	RRID:CVCL_C302
Human: UPMD2	(Griewank et al., 2012)	RRID:CVCL_C298
Human: OMM1.3	(Griewank et al., 2012)	RRID:CVCL_C306
Human: UPMM3	(Griewank et al., 2012)	RRID:CVCL_C295
Human: UPMD1	(Griewank et al., 2012)	RRID:CVCL_C297
Human: A375	ATCC	CRL-1619; RRID:CVCL_0132
Human: A2058	ATCC	CRL-11147; RRID:CVCL_1059
Human: COL800	Sigma-Aldrich	93051123; RRID:CVCL_1135
Experimental Models: Organisms/Strains		
Mouse: Tyr::CreER^{T2}: B6.Cg-Tg(Tyr-cre/ERT2)13Bos/J	The Jackson Laboratory	RRID:IMSR_JAX:012328
Mouse: BRaf^{CA}: B6.129P2(Cg)-*Braf*^{tm1Mmcm}/J	The Jackson Laboratory	RRID:IMSR_JAX:017837
Mouse: Bap1$^{flox/flox}$: Bap1$^{tm1a(EUCOMM)Hmgu}$	(LaFave et al., 2015)	RRID:MGI:5550605
Mouse: GNA11^{Q209L} (R26-LSL-GNA11_Q209L)	This paper	N/A
Mouse: CB17-SCID: C.B-*Igh-1*^{b}/IcrTac-*Prkdc*^{scid}	Taconic	RRID:IMSR_TAC:cb17sc
Mouse: R26-LSL-EYFP (B6.Cg-*Gt(ROSA)26Sor*$^{tm3(CAG-EYFP)Hze}$/J)	The Jackson Laboratory	RRID: IMSR_JAX: 007903
Oligonucleotides		

Primers; see Table S2	This paper	N/A
shRNA targeting RasGRP3; see Table S3	The RNAi Consortium ShRNA Library	MSKCC RNAi Core
Recombinant DNA		
MSCV-BRAF-V600E-HA-FLAG	This paper	Quikchange; Gateway; MSCV-HA-FLAG-puro-Dest
R777-E016 Hs.BRAF-nostop	Addgene	Addgene Plasmid #70300
MSCV-K-RAS-G12V-GFP	This paper	Gateway; MSCV-IRES-GFP-Dest
pDONR223-K-RAS V12	(Yang et al., 2011)	Addgene Plasmid #31200
GNAQ cDNA	Origene	sc128110
pBTG	(Murtaugh et al., 2003)	Addgene Plasmid #268
pRosa26PAm1	(Chen et al., 2013; Murtaugh et al., 2003)	Addgene Plasmid #15036
MSCV-puro	(Olive et al., 2009)	Addgene Plasmid #24828
MSCV-puro-GNAQ-Q209L	This paper	Quikchange; MSCV-puro
Software and Algorithms		
STAR v2.330	(Dobin et al., 2013)	
GSEA		http://software.broadinstitute.org/gsea/index.jsp
GraphPad Prism v6.0		https://www.graphpad.com/scientific-software/prism/
Partek Genomics Suite		http://www.partek.com/pgs
Cufflinks	(Roberts et al., 2011)	

Supplementary References

Bennett, D.C., Cooper, P.J., and Hart, I.R. (1987). A line of non-tumorigenic mouse melanocytes, syngeneic with the B16 melanoma and requiring a tumour promoter for growth. Int J Cancer *39*, 414-418.

Bosenberg, M., Muthusamy, V., Curley, D.P., Wang, Z., Hobbs, C., Nelson, B., Nogueira, C., Horner, J.W., Depinho, R., and Chin, L. (2006). Characterization of melanocyte-specific inducible Cre recombinase transgenic mice. Genesis (New York, NY : 2000) *44*, 262-267.

Cerami, E., Gao, J., Dogrusoz, U., Gross, B.E., Sumer, S.O., Aksoy, B.A., Jacobsen, A., Byrne, C.J., Heuer, M.L., Larsson, E., *et al.* (2012). The cBio cancer genomics portal: an open platform for exploring multidimensional cancer genomics data. Cancer discovery *2*, 401-404.

Chen, Y., Chi, P., Rockowitz, S., Iaquinta, P.J., Shamu, T., Shukla, S., Gao, D., Sirota, I., Carver, B.S., Wongvipat, J., *et al.* (2013). ETS factors reprogram the androgen receptor cistrome and prime prostate tumorigenesis in response to PTEN loss. Nature medicine *19*, 1023-1029.

Dobin, A., Davis, C.A., Schlesinger, F., Drenkow, J., Zaleski, C., Jha, S., Batut, P., Chaisson, M., and Gingeras, T.R. (2013). STAR: ultrafast universal RNA-seq aligner. Bioinformatics *29*, 15-21.

Griewank, K.G., Yu, X., Khalili, J., Sozen, M.M., Stempke-Hale, K., Bernatchez, C., Wardell, S., Bastian, B.C., and Woodman, S.E. (2012). Genetic and molecular characterization of uveal melanoma cell lines. Pigment cell & melanoma research *25*, 182-187.

LaFave, L.M., Beguelin, W., Koche, R., Teater, M., Spitzer, B., Chramiec, A., Papalexi, E., Keller, M.D., Hricik, T., Konstantinoff, K., *et al.* (2015). Loss of BAP1 function leads to EZH2-dependent transformation. Nature medicine *21*, 1344-1349.

Madisen, L., Zwingman, T.A., Sunkin, S.M., Oh, S.W., Zariwala, H.A., Gu, H., Ng, L.L., Palmiter, R.D., Hawrylycz, M.J., Jones, A.R., *et al.* (2010). A robust and high-throughput Cre reporting and characterization system for the whole mouse brain. Nat Neurosci *13*, 133-140.

Murtaugh, L.C., Stanger, B.Z., Kwan, K.M., and Melton, D.A. (2003). Notch signaling controls multiple steps of pancreatic differentiation. Proceedings of the National Academy of Sciences of the United States of America *100*, 14920-14925.

Olive, V., Bennett, M.J., Walker, J.C., Ma, C., Jiang, I., Cordon-Cardo, C., Li, Q.J., Lowe, S.W., Hannon, G.J., and He, L. (2009). miR-19 is a key oncogenic component of mir-17-92. Genes & development *23*, 2839-2849.

Roberts, A., Trapnell, C., Donaghey, J., Rinn, J.L., and Pachter, L. (2011). Improving RNA-Seq expression estimates by correcting for fragment bias. Genome biology *12*, R22.

Shin, G., Kang, T.W., Yang, S., Baek, S.J., Jeong, Y.S., and Kim, S.Y. (2011). GENT: gene expression database of normal and tumor tissues. Cancer Inform *10*, 149-157.

Subramanian, A., Tamayo, P., Mootha, V.K., Mukherjee, S., Ebert, B.L., Gillette, M.A., Paulovich, A., Pomeroy, S.L., Golub, T.R., Lander, E.S., *et al.* (2005). Gene set enrichment analysis: a knowledge-based approach for interpreting genome-wide expression profiles. Proceedings of the National Academy of Sciences of the United States of America *102*, 15545-15550.

Van Raamsdonk, C., Griewank, K., Crosby, M., Garrido, M., Vemula, S., Wiesner, T., Obenauf, A., Wackernagel, W., Green, G., Bouvier, N., *et al.* (2010). Mutations in GNA11 in uveal melanoma. The New England Journal of Medicine *363*, 2191-2199.

Wiederschain, D., Wee, S., Chen, L., Loo, A., Yang, G., Huang, A., Chen, Y., Caponigro, G., Yao, Y.-M.M., Lengauer, C., *et al.* (2009). Single-vector inducible lentiviral RNAi system for oncology target validation. Cell cycle (Georgetown, Tex) *8*, 498-504.

Yang, X., Boehm, J.S., Yang, X., Salehi-Ashtiani, K., Hao, T., Shen, Y., Lubonja, R., Thomas, S.R., Alkan, O., Bhimdi, T., *et al.* (2011). A public genome-scale lentiviral expression library of human ORFs. Nature methods *8*, 659-661.

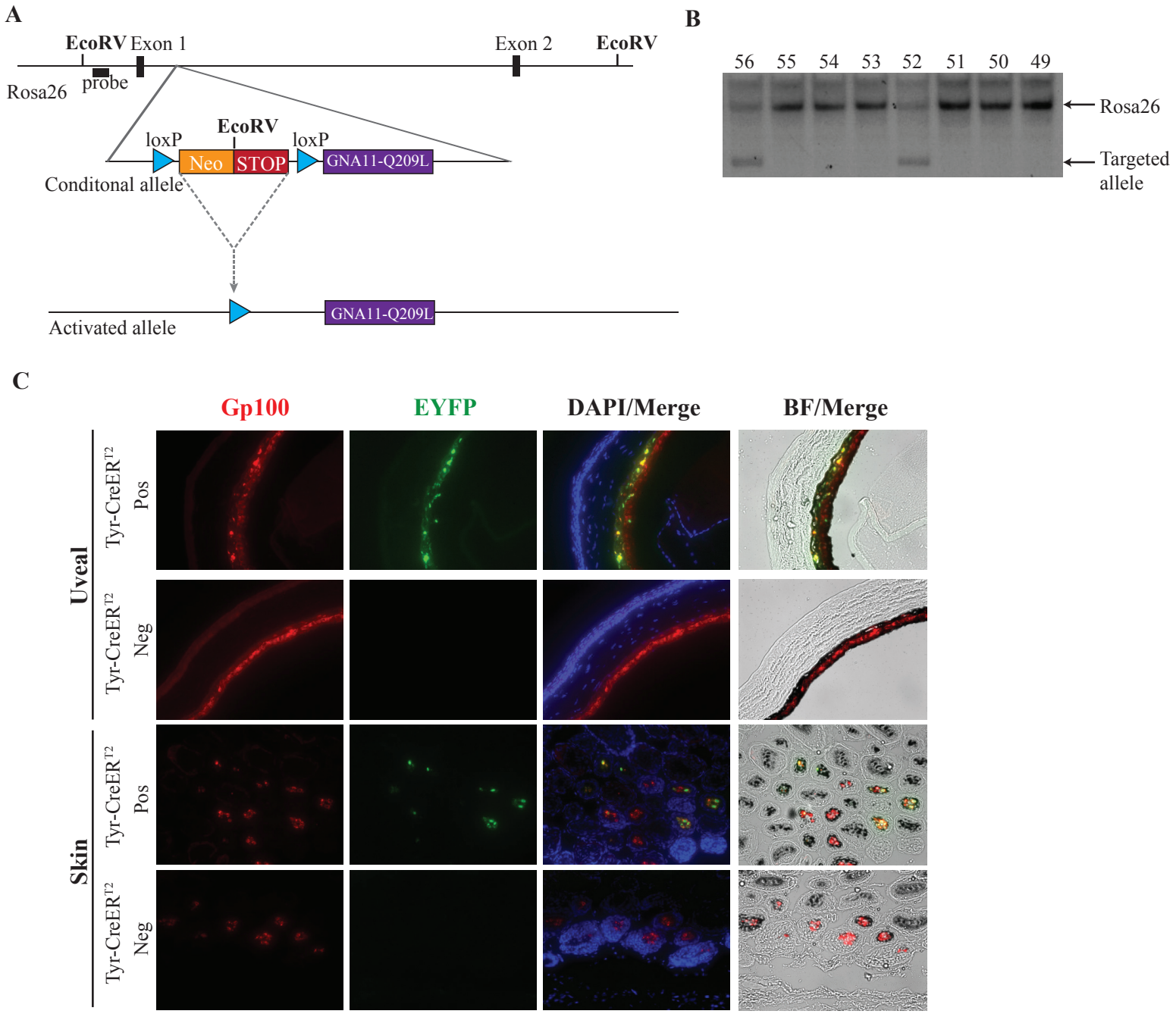

Figure S1, related to Figure 1. GNA11^{Q209L} mouse targeting

(**A**) Targeting strategy for conditional GNA11^{Q209L} allele in the *Rosa26* locus. Upon Cre-mediated recombination of the loxP, the Neo-STOP cassette is excised and GNA11^{Q209L} is expressed. Southern probe and *EcoRV* sites are indicated and targeting cassette introduces a new EcoRV site.

(**B**) Southern blot analysis using *EcoRV* and probing for 5'Rosa26. ES cell clones 56, 52 are positive for GNA11^{Q209L} allelic targetting.

(**C**) EYFP fluorescence, Gp100 immunofluorescence and bright-field images of uveal tract and skin in Tyr-CreER^{T2}; *CAG-LSL-EYFP* and control Cre-negative; *CAG-LSL-EYFP* mice 7 days after tamoxifen injection. Melanocytes are marked by Gp100-positivity as well as strong pigment readily appreciable on bright-field.

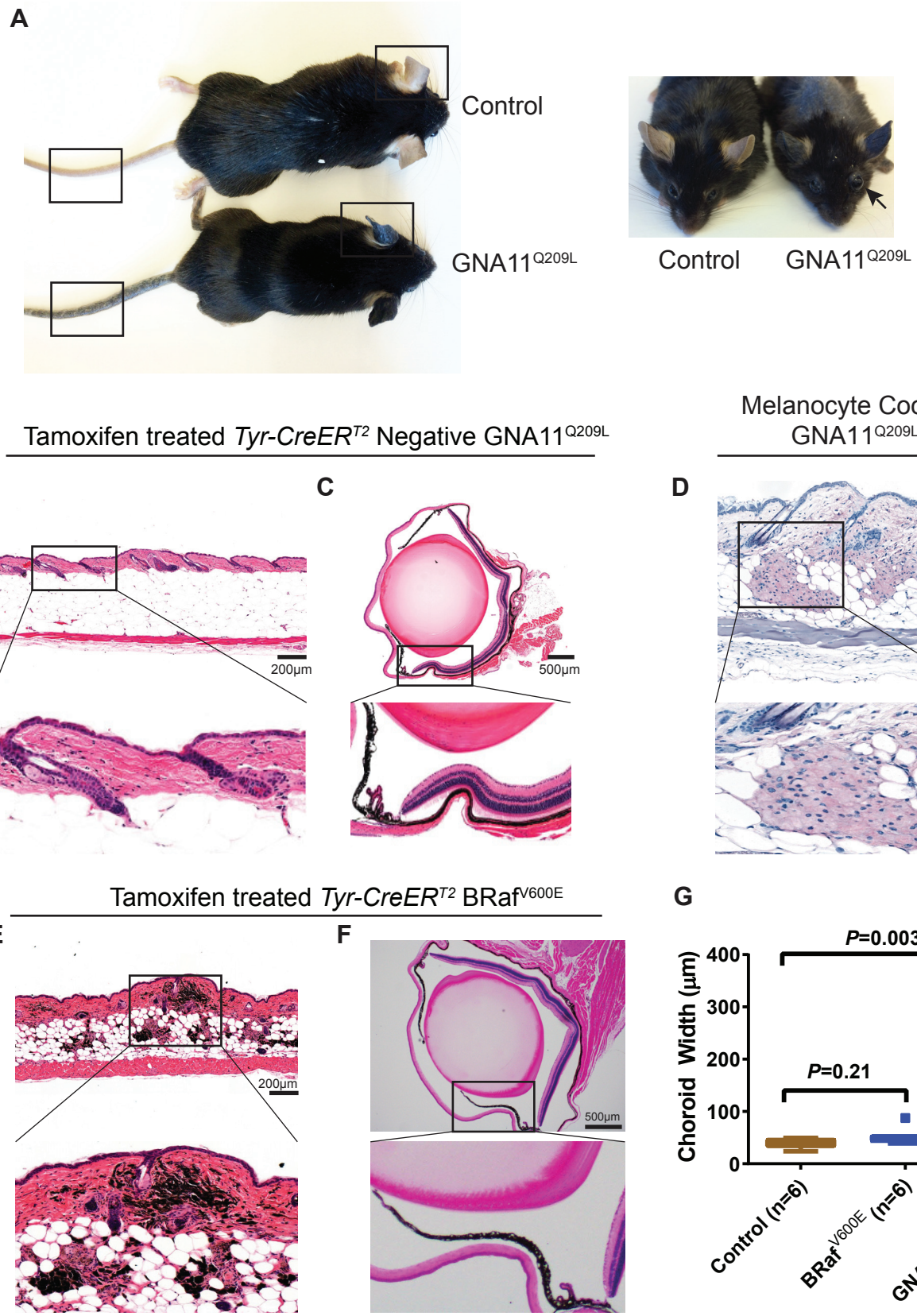

Figure S2, related to Figure 1. GNA11^{Q209L} and control mice phenotypes.

(**A**) Photographs of *Tyr-CreERT2* negative control and GNA11^{Q209L} mice 1 month after tamoxifen injection. Boxes highlight the pigmentation differences in the ears and tail. Arrow highlights the eye bulging.

(**B-C**) Representative H&E images of the skin (B) and eye (C) of a *Rosa26-LSL-GNA11^{Q209L}* (Cre-negative) mouse 12 months after tamoxifen injection.

(**D**) Immunohistochemistry of skin from a *Tyr-CreERT2; Rosa26-LSL-GNA11^{Q209L}* mouse 3 months after tamoxifen injection for melanoma cocktail (HMB45, DT101, BC199) using Red Chromogen (red) staining.

(**E-F**) Representative H&E images of the skin (**E**) and eye (**F**) of a 12-month tamoxifen treated BRaf^{V600E} mouse.

(**G**) Tukey plot of uveal width in mice of the indicated genotype 6 months after tamoxifen injection. Unpaired T-test.

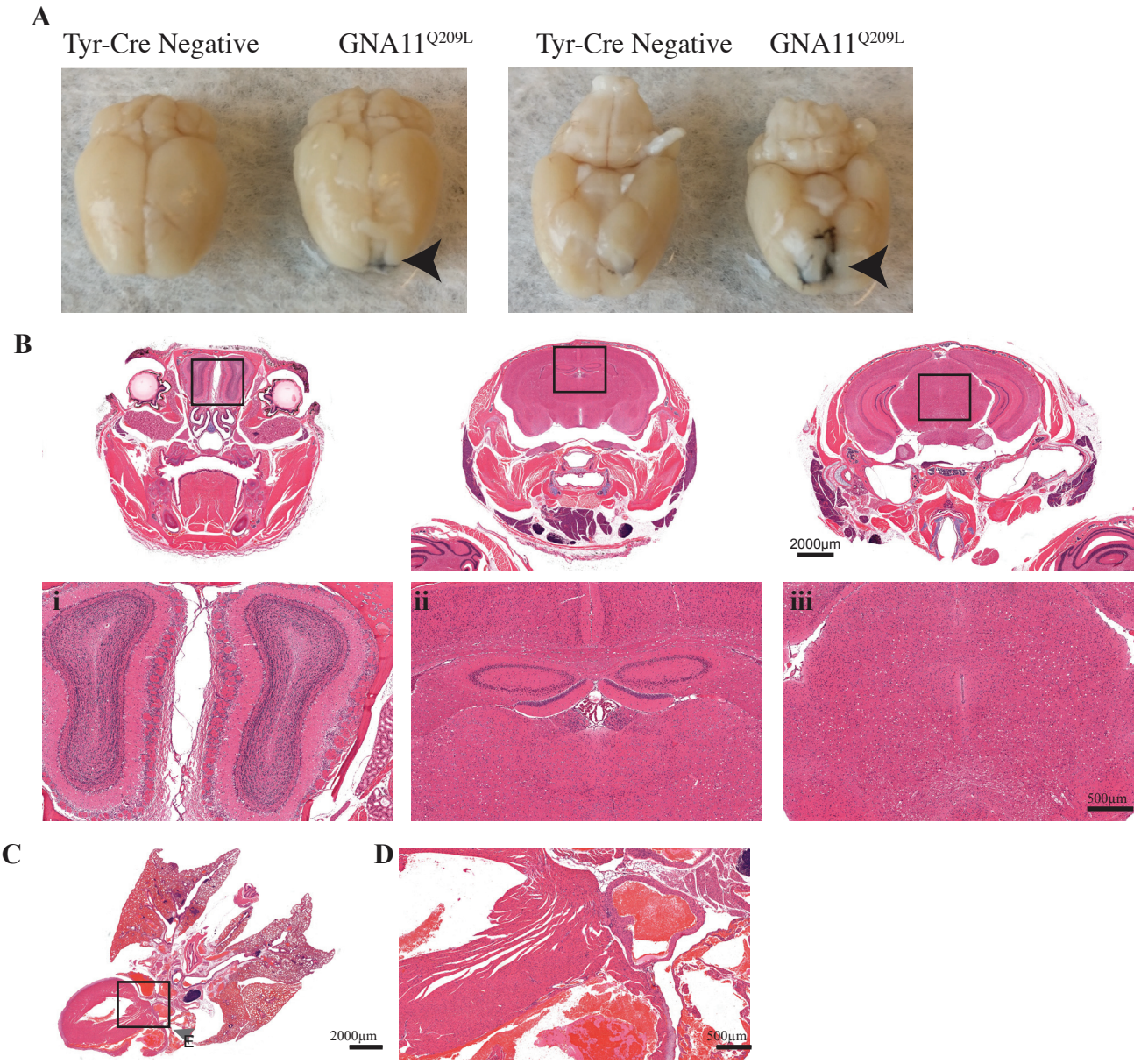

E

Months post-tamoxifen injection	<3	3-6	5-9	9+
$GNA11^{Q209L}$	1/4	8/8	4/4	2/2
Mean number of tumors (SD)	0.75 (1.5)	4.5 (2.6)	4.75 (2.6)	9.5 (3.5)
$GNA11^{Q209L}$ $Bap1^{KO}$	0/3	6/6	4/4	2/2
Mean number of tumors (SD)	0 (0)	3.8 (2)	4.25 (1.7)	8 (1.4)

Figure S3, related to Figures 2. $GNA11^{Q209L}$ CNS phenotype and controls.

(**A**) Representative images of whole brains showing focal pigmentation of the leptomeninges in $GNA11^{Q209L}$ (arrow).

(**B**) Sequential coronal skull sections (**top**), magnified images of select brain regions (**i**) olfactory bulb, (**ii**) choroid plexus of the third ventricle, (**iii**) meninges of the longitudinal fissure. Scale bar 2000µm (**top**), 500µm (**bottom**).

(**C**) Representative H&E image of heart and lung *Tyr-CreER^{T2}; BRaf^{V600E}* mice.

(**D**) Magnification of heart valve; box and gray arrowhead in (C). Scale bar 500µm.

(**E**) Prevalence of lung lesions in *Tyr-CreER^{T2}; R26-LSL-GNA11^{Q209L}* and *Tyr-CreER^{T2}; R26-LSL-GNA11^{Q209L}* mice by age post-tamoxifen injection.

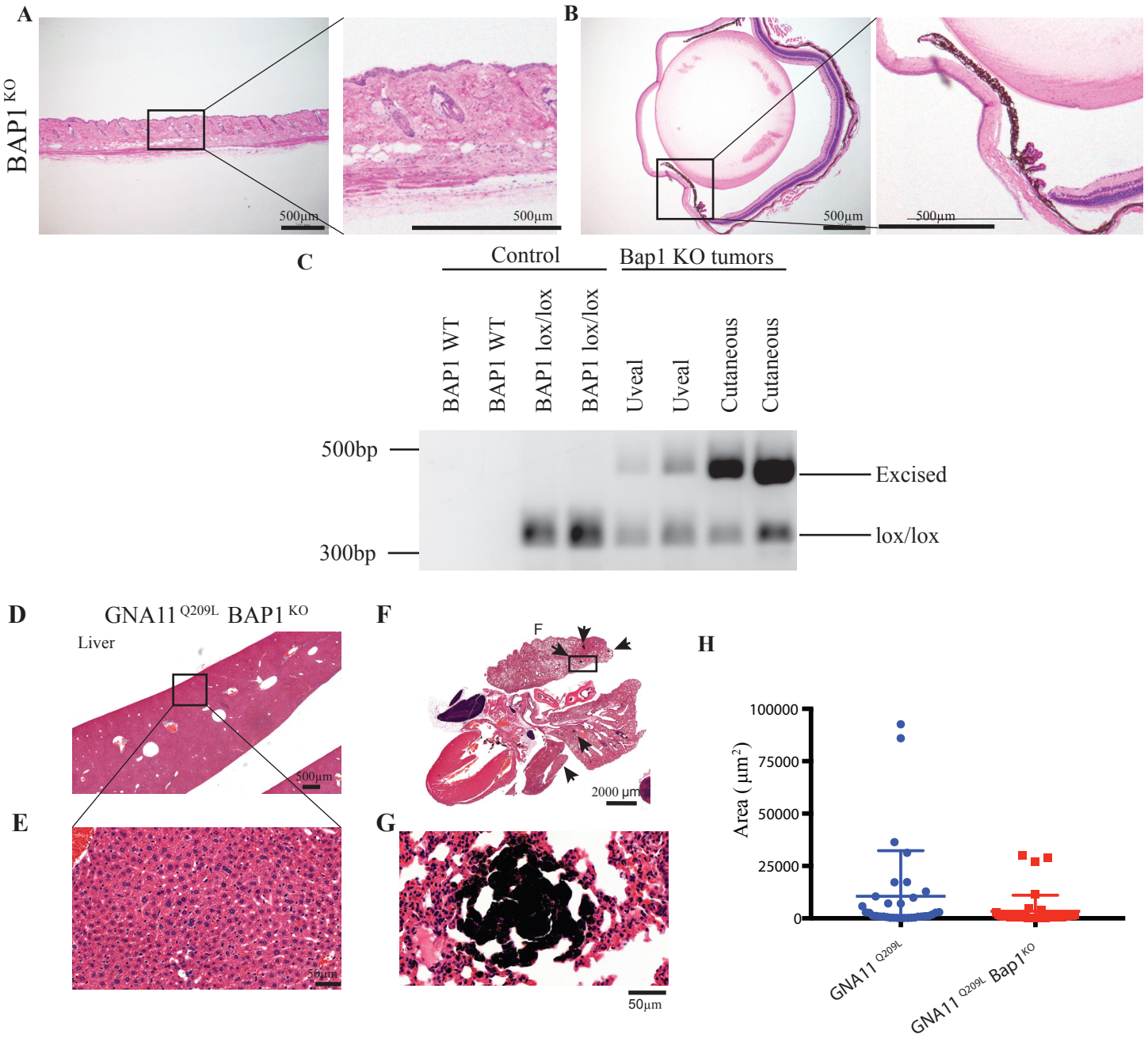

Figure S4, related to Figure 3. Bap1^{KO} mouse confirmation and histology

Representative H&E images of haired skin and subcutis (**A**) and eye (**B**) of *Tyr-CreER^{T2} Bap1^{KO}* mice 20-months post-tamoxifen injection. Scale bar 500µm.

(**C**) PCR for Bap1 lox/lox excision, controls and BAP1 KO tumors. Lox/lox amplification 327 bp and Bap1 KO (excision) 451 bp.

(**D-E**) Representative images of a GNA11^{Q209L} Bap1^{KO} mouse liver. Scale bar 500µm (D) and 50µm (E).

(**F**) Representative image of a GNA11^{Q209L} Bap1^{KO} mouse lung and heart. Scale bar 2000µm.

(**G**) Selected image of lung lesions. Image refers to box in (F). Scale bar 50 m.µ

(**H**) Quantification of lung tumor area (µm^2) in two mice per group (GNA11^{Q209L} and GNA11^{Q209L} Bap1^{KO}). Shown as scatter-dot plot; each dot represents the quantification of one tumor. Error bars; means ± s.e.m from all tumors present. *P* = ns.

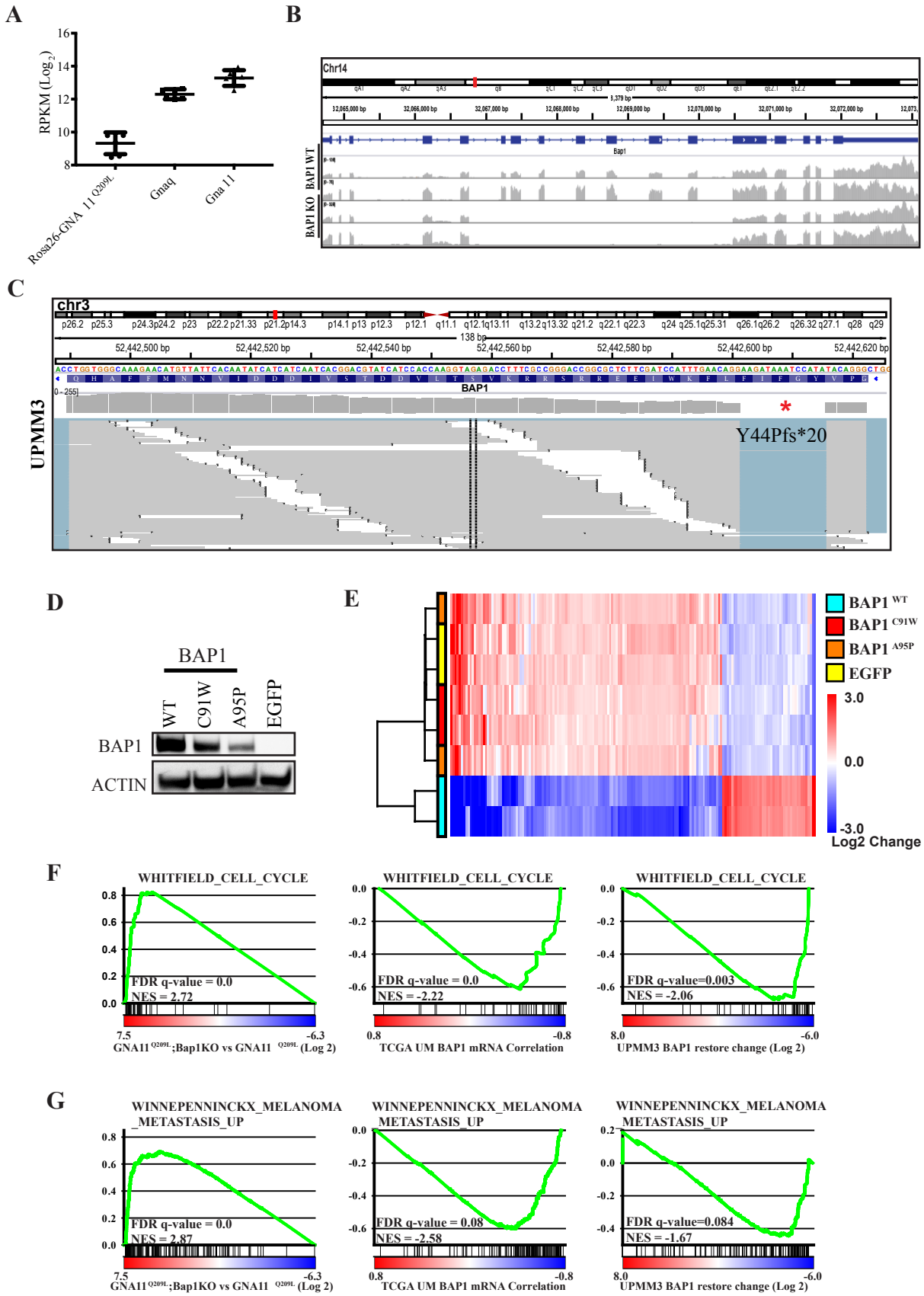

Figure S5, related to Figure 3. Bap1 RNA-sequencing reads in GNA11^{Q209L} tumors

(**A**) RNA-seq quantification of GNA11^{Q209L} positive mouse cutaneous tumors for Rosa26- GNA11^{Q209L} and endogenous *Gnaq* and *Gna11*. (**B**) Representative IGV view of RNA-seq reads at *Bap1* for GNA11^{Q209L} Bap1^{WT} and GNA11^{Q209L} Bap1^{KO} tumors showing deletion of exons 6-12. (**C**) IGV view of RNA-seq reads at *BAP1* for UPMM3 showing frameshift deletion (*). (**D**) Immunoblot of BAP1 for UPMM3 cells EGFP, BAP1 WT, BAP1 C91W and BAP1 A95P. (**E**) Hierarchial clustering of differential gene expression upon introduction of EGFP, BAP1 WT, BAP1 C91W and BAP1 A95P in duplicate. (**F**) Representative cell cycle signature (WHITFIELD_CELL_CYCLE) and (**G**) metastatic signature (WINNEPENNINCKX_MELANOMA_METASTASIS_UP) from GSEA analysis of each of three BAP1 datasets (mouse model, TCGA, and UPMM3 cell line).

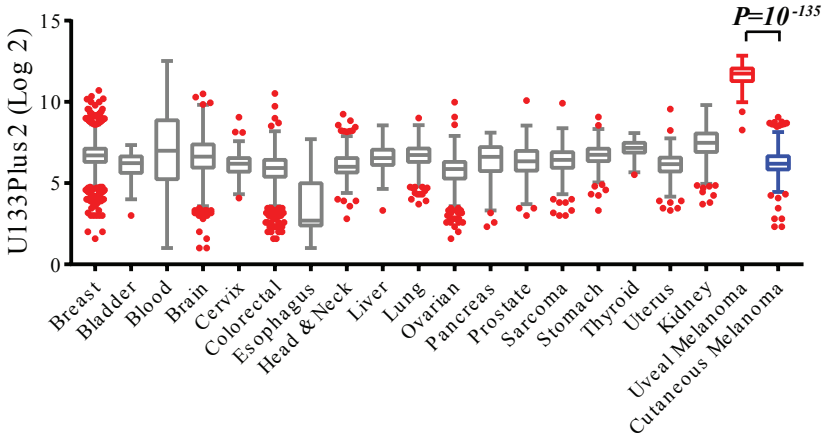

Figure S6, related to Figure 5. *RASGRP3* expression in Affymetrix U133Plus2 datasets

(**A**) Gene expression of *RASGRP3* across tumor types from the GENT (Gene Expression across Normal and Tumor tissue) U133Plus2 microarray database. Outliers shown in red dots. Uveal melanoma (red) and cutaneous melanoma (blue).

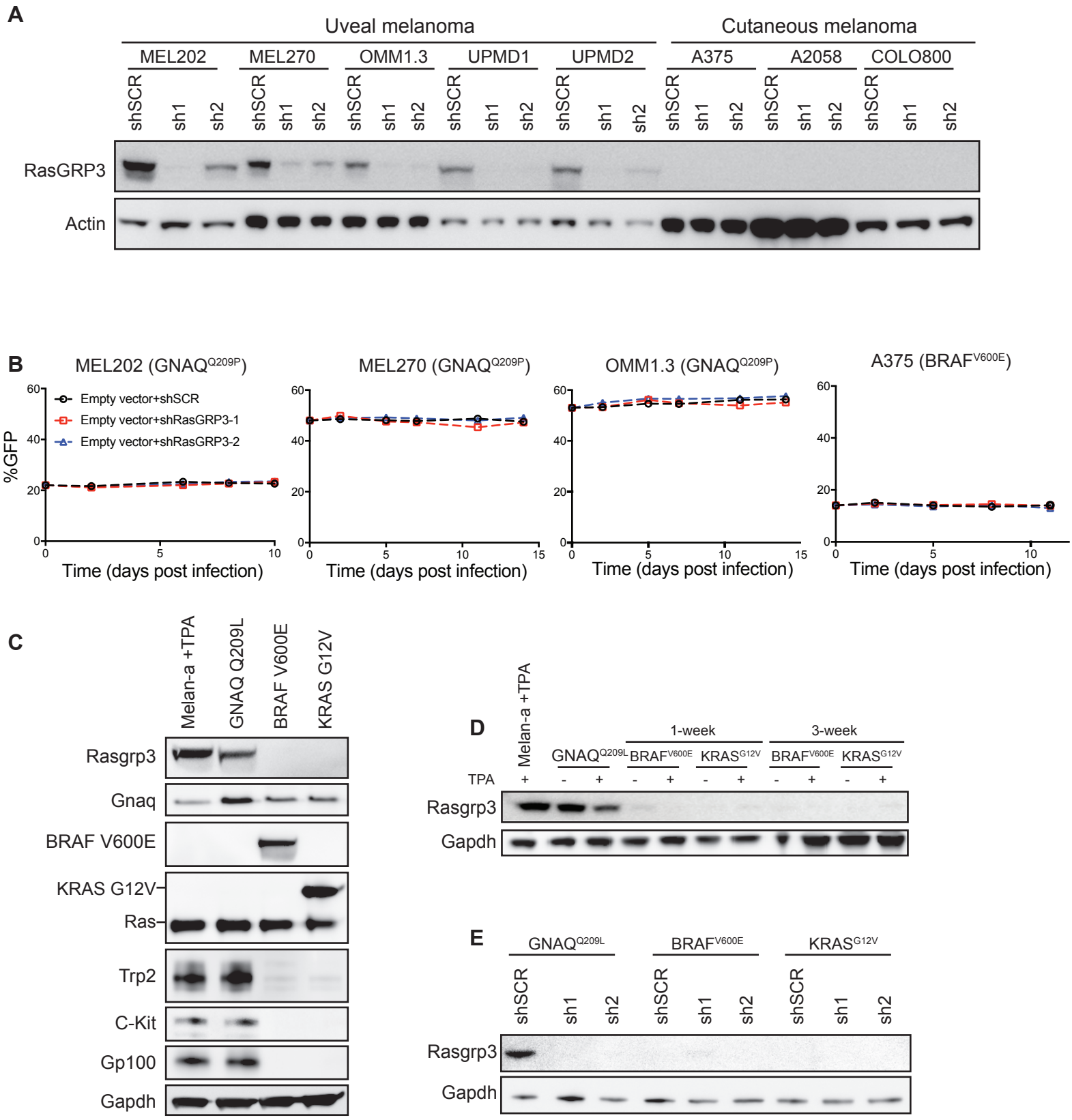

Figure S7, related to Figure 6 & 7. Depletion of RasGRP3 in panel of uveal and cutaneous melanoma cell lines
(A) Protein levels of RasGRP3 at day 3 of shRNA mediated knockdown of growth curve shown in Figure 6A-B. (**B**) Competition assay of empty vector-GFP rescue in the presence of RasGRP3 shRNA-mediated depletion. Uveal and cutaneous melanoma cells stably expressing doxycycline-inducible scrambled shRNA (shSCR) or shRNA targeting RASGRP3 (shRASGRP3-1, shRASGRP3-2) in the presence of KRASG12V-GFP. Percentage of GFP analyzed via flow cytometry over time.(**C**) Protein levels of RasGRP3 and melanocyte makers (Trp2, C-Kit and Gp100) in transduced melan-a cells with GNAQ^{Q209L}, BRAF^{V600E} and KRAS^{G12V}. (**D**) Protein levels of RasGRP3 by immunoblot at upon addition of TPA to the media of GNAQ^{Q209L}, BRAF^{V600E} and KRAS^{G12V} cells for 1- and 3-weeks, respectively. (**E**) Protein levels of RasGRP3 by immunoblot at day 3 of shRNA mediated knockdown of Rasgrp3 corresponding to the growth curve shown in Figure 7A

Table S2. Mouse genotyping primers and Quickchange primers. Related to Figures 1-3, 6-7.

Genotype primer	**Forward**	**Reverse**	**Additonal**
Tyr-Cre	CAGGGTGTTATAAGCAATCCC	CCTGGAAAATGCTTCTGTCCG	
Bap1 lox/lox	CCACAACGGGTTCTTCTGTT	ACTGCAGCAATGTGGATCTG	GAAAAGGTCTGACCCAGATCA
BRAF CA	TGAGTATTTTTGTGGCAACTGC	CTCTGCTGGGAAAGCGGC	
GNA11 Q290L	CGTGGAGAAGGTGACCACC	GATCCACTTCCTCCGCTC	
Rosa26	TCCCGACAAAACCGAAAATC	AAGCACGTT TCCGACTTGAG	
Quikchange primer	**Forward**	**Reverse**	
BRAF V600E	ccactccatcgagatttctctgtagctagaccaaaat	attttggtctagctacagagaaatctcgatggagtgg	
GNAQ Q209L	cttctctctgaccttaggccccctacatcga	tcgatgtaggggcctaaggtcagagagaag	
BAP1 excision primer	**Forward**	**Reverse**	
Bap1 KO	GCCACTGCATGGTATCTGGT	CAGGTGGCCTCCTCTACTCT	TCTTTTCCGCCTACTGCGAC

Table S3. shRNA sequences and RNAi Consortium ShRNA Library numbers. Related to Figures 6-7.

	Sequene	**The RNAi Consortium ShRNA Library #**
Human shRASGRP3-1	GCTGCAATGAATTTCGATTAA	TRCN0000048113
Human shRASGRP3-2	GCCTCAGTCATAGTTCCATTT	TRCN0000048114
Mouse shRasgrp3-1	GCCTGCCTCTTATTTGACCAT	TRCN0000022732
Mouse shRasgrp3-2	GCTGGTGTGGATGTTGTAGAT	TRCN0000022733